International Journal of Solids and Structures 97–98 (2016) 699–713

Contents lists available at ScienceDirect

International Journal of Solids and Structures

journal homepage: www.elsevier.com/locate/ijsolstr

# Analysis of dynamic damage propagation in discrete beam structures

M.J. Nieves [a,*], G.S. Mishuris [b], L.I. Slepyan [c]

[a] Mechanical Engineering and Materials Research Centre, Liverpool John Moores University, James Parsons Building, Byrom Street, Liverpool L3 3AF, UK
[b] Department of Mathematics, Aberystwyth University, Wales, UK
[c] School of Mechanical Engineering, Tel Aviv University, Tel Aviv, Israel

ARTICLE INFO

*Article history:*
Received 17 August 2015
Revised 7 January 2016
Available online 12 April 2016

*Keywords:*
Beam structures
Waves and fracture
Discrete media
Wiener–Hopf technique

ABSTRACT

In the last decade, significant theoretical advances were obtained for steady-state fracture propagation in spring-mass lattice structures, that also revealed surprising fracture regimes. Very few articles exist, however, on the dynamic fracture processes in lattices composed of beams. In this paper we analyse a failure (feeding) wave propagating in a beam-made lattice strip with periodically placed point masses. The fracture occurs when the strain of the supporting beam reaches the critical value. The problem reduces to a Wiener–Hopf equation, from which the complete solution is obtained. Two cases are considered when the feeding wave transmits into the intact structure as sinusoidal waves or only as an evanescent wave. For both cases, a complete analysis of the strain inside the structure is presented. We determine the critical level of the feeding wave, below which the steady-state regime does not exist, and its connections to the feeding wave parameters and the failure wave speed. The accompanied dynamic effects are also discussed. Amongst much else, we show that the switch between the two considered regimes introduces a rapid change in the minimum energy required for the failure wave to propagate steadily. The failure wave developing under an incident sinusoidal wave is remarkable due to the fact that there is an upper bound of the domain where the steady-state regime exists. In the present paper, only the latter is examined; the alternative regimes are considered separately.



## 1. Introduction

Lattice models are used to reveal important quasi-static and dynamic phenomena caused by both the microstructure of materials and the periodic structure of large-scale constructions. In the first analytical solutions Slepyan (1981) and Slepyan and Troyankina (1984) obtained for mass-spring lattices, the role of the microstructure in fracture and phase transition was demonstrated. In particular, it was shown that wave radiation always accompanies the steady-state dynamic crack and phase propagation (Mishuris et al., 2009a; Slepyan, 2010b; Slepyan et al., 2015; 2010). The radiation creates the speed-dependent wave resistance, which cannot be detected in a homogeneous material model (Slepyan, 2002; 2010a). This phenomena accounts for instabilities in the crack path propagation in a homogeneous material, which is attributed to the composition of its microstructure, Marder and Gross (1995), that can yield complex crack behaviour such as micro-branching and oscillation of the crack paths (Bouchbinder et al., 2010).

A discrete structure provides an effective way of building in different physical scales to describe local fracture phenomena. In this way, even the atomic-scale influences on fracture processes can be traced (Marder, 2004).

On the other hand, linear lattice structures allow one to use effective analytical techniques (such as the Fourier and Laplace transforms in conjunction with a moving coordinate system; Slepyan, 2002; 2010a) to reduce to a problem involving a Wiener–Hopf equation (Noble, 1958) set along the axis of the crack. This equation contains a term corresponding to the load applied to the structure. One can specify the set of remote loads (see Slepyan, 2002) and generate the corresponding analytical solutions to this equation, which contain information on the dynamic features of various propagation regimes. Constant and oscillatory loads can be embedded into such equations and readily solved to reveal very different dynamical fracture regimes. A collection of such solutions for the mass-spring lattice structures, with different geometries (having square or triangular unit cells), can be found in Slepyan (2001a, 2002), Mishuris et al. (2009a, 2009b) and Slepyan et al. (2010) and for homogeneous structures see Slepyan et al. (2015).

Conventional materials under various loads may also induce other interesting fracture patterns. In this sense, we refer to Deegan et al. (2003), where experiments conducted on single-crystal silicon strips under thermal loading with high temperature gradient may produce straight line, wavy or multi-branched cracks.

* Corresponding author. Tel.: +44 151 231 2011.
*E-mail address:* M.J.Nieves@ljmu.ac.uk (M.J. Nieves).

http://dx.doi.org/10.1016/j.ijsolstr.2016.02.033
0020-7683/

A similar method to that presented in Slepyan (2002) can be utilised to model a bridged crack propagating within a lattice (Mishuris et al., 2008b) or the dynamical extraction of a thread from the lattice (Mishuris et al., 2008a). The techniques are also applicable to the analysis of cracks propagating at speeds within subsonic, intersonic and supersonic regimes (Guozden et al., 2010; Slepyan, 2001b) where changes occur in the lattice response in the vicinity of the crack tip when moving between speed regimes. Brittle fracture propagation in finite triangular mass-spring systems has been analysed in Behn and Marder (2015), along with change in the local crack tip behaviour during the transition from subsonic to supersonic regimes.

Other defects such as structured interfaces can be incorporated, through adjustment of several local material properties within a lattice. These defects may then play a role in promoting or hindering the propagation of flaws within a lattice as shown in Mishuris et al. (2012). Cracks propagating through inhomogeneous elastic lattices can also be treated by the same approach in Nieves et al. (2013).

Summarising, there exist many articles concerning the analytical solution to fracture and phase transition problems in periodic mass-spring lattices, however, there are few for beam-made periodic structures. The static problem of a crack within a beam-made square cell lattice has been considered in Ryvkin and Slepyan (2010) where bending modes of fracture in a beam-made lattice were analysed.

In the case of failure waves inside a massless beam structure, a simplified model of a bridge was analysed (Brun et al., 2013). There, models of a failure wave propagating in uniformly and discretely supported beams under gravity forces were also compared. Failure was assumed to propagate with constant speed and is represented by the drop in stiffness of the elastic supports after the strain at the transition front reaches a critical value. Further, this model has been applied to the analysis of the progressive collapse of the San Saba bridge (Movchan et al., 2015), and the collapse rate of this bridge can be accurately predicted by the model.

Models of fracture in periodic structures may have applications to very important phenomena such as the progressive collapse of a civil engineering structure. Engineering studies of this phenomena have been used to analyse the collapse of the Twin Towers, World Trade Centre, New York, on 9/11 (Bažant et al., 2007). Some discussions of progressive collapse in the case of bridges as a result of localised damage or unwanted vibrations caused by natural disasters such as earthquakes can be found in Kawashima et al. (2009) and Liu et al. (2011). Collapse of the several bridges due to the catastrophic Wenchuan earthquake, China, in 2008 has been reported in Kawashima et al. (2009).

As another example, in Fig. 1 we show the result of spontaneous progressive collapse of house roofing in Tottenham, London, U.K., 2014. The rooftop is composed of support rafters that attach to the walls of the house (along the dashed line at 3) and to a ridge beam at the roof apex. The damage has been initiated at the point 1a. where the ridge beam was connected to one of the neighbouring houses. After this, the ridge beam drops from this point suddenly and as a result the supporting rafters along ridge beam are progressively pushed outward as the damage propagates to 2. The collapse has also led to the damage of connections between the base of the rafters and the house walls (their original position marked with the dashed line at 3), leaving a substantial part of the rooftop hanging over the house walls. The damage process that can be characterised by the result of transverse movement of the ridge beam that brings about the damage of the connections between the support rafters and the house at the dashed line 3. This process can be linked to the propagation of fracture of the transverse supports of a discrete structure within a rigid interface as a result of transverse movement of the central beam, see Fig. 2.


**Fig. 1.** The collapse of a roof in Tottenham, U.K., 2014. Picture from http://www.tottenhamjournal.co.uk/news/lunchbreak_saves_lives_of_builders_in_tottenham_roof_collapse_1_3858222.

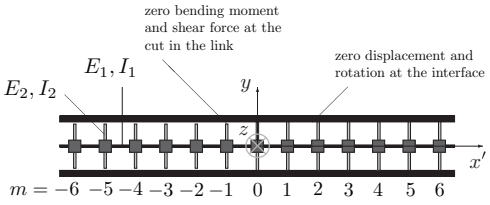


**Fig. 2.** A heterogeneous discrete structure composed of massless beam members of length $a$ with concentrated masses $M$ at the nodes $m \in \mathbb{Z}$. Members aligned with the horizontal (vertical) axis have Young's modulus $E_1$ ($E_2$) and second moment of area $I_1$ ($I_2$). Here we show a static situation, where it is permissible to number the nodes using the index $m \in \mathbb{Z}$. Later, when we consider the propagation of the transition front with a constant speed $V$ through the structure, the transition front can be traced with the moving coordinate $\eta = m - Vt/a$. In this case the variable $\eta$ replaces $m$ (with $\eta = 0$ representing the position of this front).

We note that the rooftop considered in Fig. 1 is one example of the failure of a beam structure. The focus of the current article is not to analyse the failure mechanisms of this rooftop, but to understand such a phenomenon in a structure such as in Fig. 2, which is closely linked to the collapse of buildings, long rooftops and bridges amongst many others.

Civil engineering structures considered in Bažant et al. (2007), Kawashima et al. (2009) and Liu et al. (2011) are also known as multi-structures. Understanding their performance when in operation and their failure mechanisms is of great importance. An exposition into the asymptotic theory of boundary value problems for finite multi-structures (without failure mechanisms though) has been given in the monograph (Kozlov et al., 1995), with applications to problems in electrostatics, hydrodynamics, structural mechanics and in particular fracture mechanics.

An alternative analysis of multi-structures, again without failure, involves the multi-scale asymptotic homogenisation approach presented in Panasenko (2005). This approach encapsulates the effects brought about by the microstructure, similar to the discrete periodic lattice approach presented here, in Slepyan (2002) and references therein. In dynamic problems, homogenisation is frequency dependent and efficient methods have been developed to treat high frequency regimes (Craster et al., 2010).

In the present paper, we consider a similar structure as in Ryvkin and Slepyan (2010), Brun et al. (2013) and Movchan et al. (2015) but assume a failure wave propagation under a sinusoidal incident wave. The appeal of such structures is that they are more commonly found in applications than those formed by springs. For the first time, the steady dynamic fracture of a beam structure is considered here. In accordance with Slepyan et al. (2015), we expect that there exists a domain inside some parameter space

where the steady-state solution is realised. While analysing the steady-state fracture response gives us a good description of associated phenomena, non-physical solutions associated with this model provide information of when such regimes do not exist. In addition, there may be different loading on the structure and since the problem is nonlinear, the response may be different. We therefore restrict ourselves to considering sinusoidal loading, which is very typical of such problems. Note that the phenomena corresponding the sinusoidal loading differs much from those for the invariable load (as was discussed in Slepyan et al., 2015). In particular, in the steady-state regime, the transition wave speed coincides with the incident wave phase speed independently of its amplitude and frequency, and this limits the domain where such a regime can exist. Here the transition wave under the action of a sinusoidal incident wave can propagate steadily only if the group velocity of the latter exceeds the phase speed, which is characteristic for a bending wave. In addition, for the considered problem, the lattice periodicity, along with the beam-related mode of the interaction and the wave action are completely incorporated for the first time.

The structure of the article is as follows. In Section 2 we formulate the dynamic fracture problem for discrete beam strip, as shown in Fig. 2, composed of massless beams and periodically placed masses. Section 3 contains the governing equations and associated solutions for the massless beams necessary for further analysis. We also present the equations for the balance of shear forces and moments at nodal points inside the strip, which are then converted in terms of displacements and rotations at each node in Section 3.2. Following this, in Section 3.2, the problem is reduced to a Wiener–Hopf equation. The dispersion relations for the structure are presented. The general solution of this Wiener–Hopf equation is derived in Section 4 for a general speed of the fracture transition front, while also assuming a sinusoidal feeding wave provides energy to the front. In addition to this, Section 4 also contains the analytical description of the dynamic properties of the structure. In Section 5, the distribution of the feeding wave energy amongst the other dynamic features in the structure is considered, and this is followed by conclusions in Section 6. Finally, some technical derivations of the results presented here are given in Appendix A.

## 2. The problem formulation

We consider the discrete structure as in Fig. 2, composed of massless beams connecting periodically placed point masses along the central axis of the structure (along the $x'$-axis). Each node is identified with an integer $m \in \mathbb{Z}$ and at these nodes the masses are assumed to have mass $M$. The beam connections emanating from each mass have length $a$, and the longitudinal beams have Young's modulus $E_1$ and second moment of area $I_1$. In what is considered below, transverse beams inside the structure have contrasting material properties to the longitudinal beams, and have Young's modulus $E_2$ and second moment of area $I_2$.

Equations governing the structure will be completely written in terms of the displacements $w_m(t)$ and the rotations $\theta_m^x(t)$ of the node at $m$. Bending moments and shear forces inside the $m$th longitudinal beam are denoted by $\mathcal{M}_m^x(x,t)$ and $\mathcal{V}_m^x(x,t)$. Here, $x = x' - am$ is the local coordinate in the $m$th beam and $0 < x < a$. By symmetry of the structure we restrict our attention to the shear force $\mathcal{V}_m^y(y,t)$ inside the $m$th transverse beam having local coordinate $y$, $0 < y < a$, when considering the balance of shear forces in Section 3.1. The positive directions of the bending moments in the horizontal and vertical directions of the structure are shown in Fig. 3.

In Fig. 2, the case $m = 0$ represents the interface between broken structure (without transverse supports, $m < 0$) and the intact structure (with transverse supports, $m \geq 0$). In the considered problem, fracture is assumed to occur inside the transverse beams (symmetric about the longitudinal axis) and propagate with speed $V$ inside the structure. Thus the transition front at some time $t$ can be located at $m = k(t)$, $k(t) \in \mathbb{Z}$ and can move a distance $a$ within the structure to the right, after the time interval $a/V$. As the transition front moves, the broken structure can be identified by the inequality $m < Vt/a$ and the intact structure corresponds to $m > Vt/a$. Later we will introduce the moving coordinate $\eta = m - Vt/a$ as in Slepyan (2002), for which $\eta \geq 0$ represents the intact structure and $\eta < 0$ will represent the broken structure.

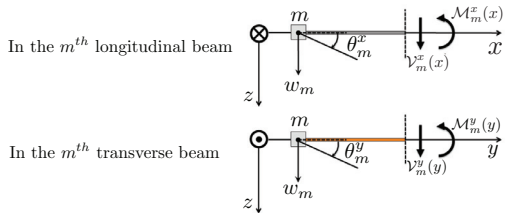


**Fig. 3.** Positive directions of displacements, rotations, moments and shear forces within elements of the structure in Fig. 2.

Fracture occurs inside the structure as follows. Let $w_c$ be the critical displacement for fracture of the transverse links inside the structure to occur. Suppose at a particular time, the transition front is at the mass $m = k$, $k \in \mathbb{Z}$ (corresponding to $\eta = 0$). When the displacement associated with the considered mass, $w_k(t)$, satisfies $w_k(t) = w_c$, the transition front moves to the mass associated with $m = k + 1$. For steady-state fracture, in addition to this condition one must also impose that the displacements ahead of the transition front do not reach the fracture criterion $w_c$. Therefore, we assume that

$$w_k(t) = w_c, \quad w_j(t) < w_c, \quad j > k, \tag{1}$$

where $k \in \mathbb{Z}$ represents the node position of the transition front at time $t$. It is worth noting that any solution violating the preceding condition provides interesting information about when non-steady fracture regimes can occur.

Connections will be derived later on the critical displacement $w_c$ in order for the steady-state solution to exist. Several scenarios for the fracture of the transverse links are possible. In Fig. 2, the fracture occurs directly at the interfaces above and below the structure. It is shown later that the equations governing the structure are independent of where the breakage occurs, provided that the symmetry of the structure is maintained.

## 3. Governing equations, dispersive nature of the structure and solution to the problem

Here, we consider the governing equations for the massless beam structure in Fig. 2. First, we introduce the fundamental relations for the beam connections inside the structure in Section 3.1. Then governing equations for the masses in the beam structure are considered in Section 3.2 and this is shown to reduce to a Wiener–Hopf equation from which the dispersive nature of the structure is identified. We present the solution to this Wiener–Hopf problem in Section 4 and this is used to provide a full description of the dynamic features of the structure that occur during the steady-state fracture process.

### 3.1. Fundamental equations for the massless beam

We compute expressions for the displacements inside the beams that will be used to construct the governing equations in

terms of the displacements and rotations of the $m$th node in the next section.

For the massless Bernoulli–Euler beam model, from the equation

$$\frac{\partial^4 W(x,t)}{\partial x^4} = 0 \tag{2}$$

and the boundary conditions

$$W(0,t) = w_m(t), \quad \frac{\partial W}{\partial x}(0,t) = \theta_m^x(t),$$
$$W(a,t) = w_{m+1}(t), \quad \frac{\partial W}{\partial x}(a,t) = \theta_{m+1}^x(t), \tag{3}$$

we have

$$W(x,t) = \left[2(w_m(t) - w_{m+1}(t)) + a(\theta_m^x(t) + \theta_{m+1}^x(t))\right]\frac{x^3}{a^3} + \left[3(w_{m+1}(t) - w_m(t)) - a(\theta_{m+1}^x(t) + 2\theta_m^x(t))\right]\frac{x^2}{a^2} + \theta_m^x(t)x + w_m(t), \tag{4}$$

where the rotation, bending moment and transverse force are defined as

$$\theta = \frac{\partial W(x,t)}{\partial x}, \quad \mathcal{M} = -EI\frac{\partial^2 W(x,t)}{\partial x^2}, \quad \mathcal{V} = -EI\frac{\partial^3 W(x,t)}{\partial x^3}. \tag{5}$$

The expressions in (4) and (5) can be used for both the longitudinal beams and the transverse beams (substituting the respective boundary conditions at $y = 0$ and $y = a$). Also recall for the longitudinal (transverse) links $E = E_1(E_2)$ and $I = I_1(I_2)$. Note that if a transverse massless beam is broken it does not influence the longitudinal structure's dynamics. For the intact transverse beams we state the following conditions:

$$W = \theta = 0 \text{ (at the interface)},$$
$$W = w_m, \theta = 0 \text{ (at the central longitudinal beam)}, \tag{6}$$

which leads to expressions for $W$ inside the intact transverse beams:

$$W(y,t) = 2w_m(t)\frac{y^3}{a^3} - 3w_m(t)\frac{y^2}{a^2} + w_m(t) \quad \text{(above the central longitudinal beam)}, \tag{7}$$

and to determine the displacement in the transverse beam below the $m$th node in the intact part, we replace $y$ by $a - y$ in (7).

We note that if the beams composing the structure were to have non-negligible density then the representations (4) and (7) are no longer valid as a result of the incorporation of a dynamic term in (2).

### 3.2. Governing equations for the massless beam structure

Here we construct the governing equations for the problem under consideration using the expressions for the displacements inside the $m$th longitudinal and transverse beams derived in the previous section. The dynamic equation in terms of the balance of shear forces at the $m$th node is

$$\mathcal{V}_m^x(0,t) - \mathcal{V}_{m-1}^x(a,t) + (\mathcal{V}_m^{y,\text{top}}(0,t) - \mathcal{V}_m^{y,\text{bottom}}(a,t))H(m - Vt/a) - M\frac{\mathrm{d}^2 w_m(t)}{\mathrm{d}t^2} = 0, \tag{8}$$

where $M$ is the mass of the node at the $m$th junction. Here $\mathcal{V}_m^x(x,t)$ is the shear force in the $m$th horizontal beam and $\mathcal{V}_m^{y,\text{top}}(y,t)$ ($\mathcal{V}_m^{y,\text{bottom}}(a,t)$) is the shear force in the transverse beams above (below) the $m$th mass in the intact region.

Here we do not take into account the moment of inertia of the mass, and so the balancing of the moments gives

$$\mathcal{M}_m^x(0,t) - \mathcal{M}_{m-1}^x(a,t) = 0. \tag{9}$$

We now consider the steady-state problem, where the free longitudinal beam with the point masses are placed at $\eta = m - Vt/a < 0$ (with the assumption that the speed $V = \text{const}$), and the supported one is placed at $\eta \geq 0$.

According to (4) and (5), we have

$$\mathcal{V}_m^x(x,t) = -\frac{6E_1I_1}{a^3}\{2(w_m(t) - w_{m+1}(t)) + a(\theta_m^x(t) + \theta_{m+1}^x(t))\}, \tag{10}$$

$$\mathcal{M}_m^x(x,t) = \frac{2E_1I_1}{a^3}\{3(a-2x)(w_m(t) - w_{m-1}(t)) + a(a-3x)(\theta_{m+1}^x(t) + \theta_m^x(t)) + a^2\theta_m^x(t)\} \tag{11}$$

whereas from (5) and (7), if $m \geq Vt/a$

$$\mathcal{V}_m^{y,\text{top}}(0,t) = -\frac{12E_2I_2}{a^3}w_m(t) \quad \text{and} \quad \mathcal{V}_m^{y,\text{bottom}}(a,t) = \frac{12E_2I_2}{a^3}w_m(t). \tag{12}$$

Next we introduce the normalisation that $V = \sqrt{E_1I_1/Ma}\,v$, where $v$ is the dimensionless speed and use (8)–(12) together with the assumption

$$w_m(t) = w(m - Vt/a), \quad \theta_m^x(t) = \theta^x(m - Vt/a). \tag{13}$$

to obtain the following equations:

$$6\{2[2w(\eta) - w(\eta-1) - w(\eta+1)] + a[\theta^x(\eta+1) - \theta^x(\eta-1)]\} + 24rw(\eta)H(\eta) + v^2\frac{\mathrm{d}^2 w(\eta)}{\mathrm{d}\eta^2} = 0, \tag{14}$$

and

$$3[w(\eta+1) - w(\eta-1)] - a[\theta^x(\eta+1) + \theta^x(\eta-1) + 4\theta^x(\eta)] = 0, \tag{15}$$

where

$$r = E_2I_2/(E_1I_1) \tag{16}$$

is a dimensionless parameter which governs the contrast in material properties in orthogonal directions inside the structure. We note that when the bending moments appearing in (9) are zero, in addition to the rotations of each mass, problem (14) and (15) reduces to the familiar one-dimensional fracture problem of the spring structure in an interface, arranged as in Fig. 2.

As suggested by (14), the transverse connections act as spring supports. This effect is general and independent of how the transverse beams are connected at the periodically placed masses along the central axis. In the present case, one could replace the transverse beam connections by an equivalent spring with stiffness $\varkappa = 24E_2I_2/a^3$.

In addition to (14) and (15), for steady-state fracture, we impose

$$w'(+0) < 0, \tag{17}$$

which ensures the displacement of the central axis of the structure, ahead of the transition front, does not increase past the critical displacement (see (1)).

Note for a homogeneous beam structure ordered as in Fig. 2, $r = 1$. Next we introduce the Fourier transform with respect to $\eta$ as

$$w^{\mathrm{F}}(k) = \int_{-\infty}^{\infty} w(\eta)e^{\mathrm{i}k\eta}d\eta, \quad \text{and} \quad \theta^{x\mathrm{F}}(k) = \int_{-\infty}^{\infty} \theta^x(\eta)e^{\mathrm{i}k\eta}d\eta, \tag{18}$$

where the dimensionless wavenumber $k = \tilde{k}a$ ($\tilde{k}$ is the original wavenumber). This transform is taken in Eqs. (14) and (15).

Let $\hat{w}^{\mathrm{F}} = w^{\mathrm{F}}/a$ which is a dimensionless quantity, the Fourier transform of (15) with respect to $\eta$ leads to

$$\theta^{x\mathrm{F}} = -\frac{3\mathrm{i}\sin k}{2 + \cos k}\hat{w}^{\mathrm{F}} \tag{19}$$

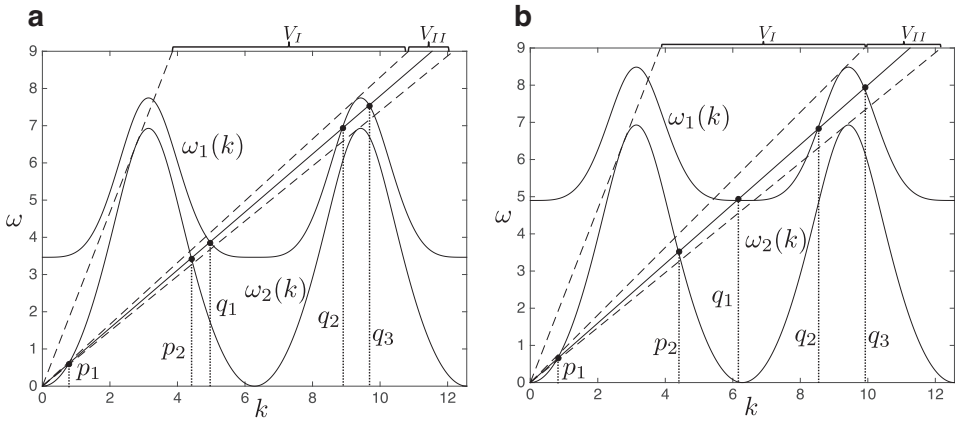


**Fig. 4.** (a) Dispersion relations $\omega_j(k)$, $j = 1, 2$, plotted as functions of the dimensionless wavenumber $k$, when (a) $r = 0.5$ and (b) $r = 1$. In (a) the line $\omega = kv$, for $v = v_1, 0.78, 0.83$ and $v_2$, is presented and in (b) the same line is given for $v = v_1, 0.8, 0.909$ and $v_2$. The dashed lines indicate the limits of the gradient $v$ of the lines, which are also limits of the speed regimes $V_I$ and $V_{II}$, (see Section 3.2.2). The solid black rays corresponding to (a) $v = 0.78$ and (b) $v = 0.8$ are shown, that indicate $p_j$, $j = 1, 2$, as the zeros of $g_2(k)$ and $q_i$, $1 \le i \le 3$, as the zeros of $g_1(k)$.

and consequently from (14) we receive

$$6\left\{4(1-\cos k) - \frac{6\sin^2 k}{2+\cos k}\right\}\hat{w}^{\mathrm{F}} + 24r\hat{w}_+ + (0+\mathrm{i}kv)^2\hat{w}^{\mathrm{F}} = 0, \tag{20}$$

where the one-sided transforms $\hat{w}_\pm$ are defined through

$$a\hat{w}_\pm = w_\pm(k) = \int_{-\infty}^{\infty} \tilde{w}(\eta)H(\pm\eta)\mathrm{e}^{\mathrm{i}k\eta}\,\mathrm{d}\eta\,, \tag{21}$$

and $0 + \mathrm{i}kv = \lim_{\varepsilon\to+0}\varepsilon + \mathrm{i}kv$. This limit corresponds to the steady-state solution as the limit that is in accordance with the causality principle (see Slepyan, 2002). In what follows, we omit the hat $\hat{}$ occurring in the above the quantities in (21).

The Wiener–Hopf equation, without the incorporation of an external load, then follows as

$$g_1(k)w_+(k) + g_2(k)w_-(k) = 0 \tag{22}$$

with

$$g_1(k) = \frac{12(1-\cos k)^2}{\cos k + 2} + 24r + (0+\mathrm{i}kv)^2, \tag{23}$$

$$g_2(k) = g_1(k) - 24r, \tag{24}$$

and the contrast parameter $r$ is defined in (16).

*3.2.1. Dispersion relations for the beam structure*

The dispersion relations for the structure can be found by setting $\omega = kv$ as in Slepyan (2002), with $\omega$ being the dimensionless angular frequency ($\tilde{\omega} = \tilde{k}V = \sqrt{E_1 I_1/Ma^3}\,\omega$ is the actual angular frequency), and solving $g_j(k) = 0$, $j = 1, 2$, which leads to

$$\omega_1(k) = \sqrt{\frac{12(1-\cos(k))^2}{\cos(k)+2} + 24r} \quad (\text{when } g_1(k) = 0) \tag{25}$$

and

$$\omega_2(k) = \sqrt{\frac{12(1-\cos(k))^2}{\cos(k)+2}} \quad (\text{when } g_2(k) = 0). \tag{26}$$

The dispersion relations (25) and (26) are plotted in Figs. 4 and 5 as functions of the normalised wavenumber $k$, for the case when $r = 0.5, 1, 1.5$ and 4. The ray $\omega = kv$ is also plotted in these figures for various speeds. The intersection of the ray $\omega = kv$ with $\omega_1(k)$ ($\omega_2(k)$) represents a wave propagating to the right (left) of the transition front within the structure. Direct comparison of the group velocity of the wave $v_g = \mathrm{d}\omega_1(k)/\mathrm{d}k$ ($\mathrm{d}\omega_2(k)/\mathrm{d}k$) at these intersection points with the phase speed $v$ indicate which waves will reach the transition front. At intersections of $\omega = kv$ with $\omega_1(k)$ ($\omega_2(k)$), if $v_g > v$ ($v_g < v$) then the corresponding waves will propagate away the transition front, otherwise they will propagate towards this front if $v > v_g$ ($v_g > v$).

*3.2.2. A particular speed range and associated fracture phenomena*

As an example, we consider the dimensionless speed in the range $v_1 < v < v_2$, with $v_1 = 0.74$ and $v_2 = 2.335$. According to the dispersion diagrams, in this speed range the function $g_2(k)$ will only have a double zero at $k = 0$ and two pairs of simple zeros at $\pm p_1$, $\pm p_2$ (see the intersections of the solid line $\omega = kv$ with the function $\omega_2(k)$ in Figs. 4 and 5). We will see that the considered speed range for $v$ can also be partitioned into two speed ranges defined by sets $V_I$ and $V_{II}$:

$$\begin{aligned} V_I &:= \{v : g_1(k) = 0 \text{ for } k = \pm q_1,\ q_1 \neq 0\ \}, \\ V_{II} &:= \{v : g_1(k) = 0 \text{ for } k = \pm q_j,\ 1 \le j \le 3, \\ &\qquad q_j \neq 0 \text{ and are distinct}\}. \end{aligned} \tag{27}$$

If the speed $v < v_1$, then the same concepts are extendable to this case. There, one may expect the density of sets representing various collections of zeros of $g_j$, $j = 1, 2$, to increase and the procedure developed here can be applied to these cases.

For $v \in V_I$, the pair of simple zeros of $g_1(k)$ is denoted by $\pm q_1$, whereas for $v \in V_{II}$, in addition to these zeros we have two more pairs of simple zeros at $k = \pm q_2, \pm q_3$. Examples of when the speed $v$ is chosen so that $v \in V_{II}$ can be found in Fig. 4, whereas when $v \in V_I$ an example is shown in Fig. 5(a) and (b). The behaviour of the wave numbers $p_i$, $i = 1, 2$, and $q_j$, $1 \le j \le 3$ as a function of $v$ can be found in Fig. 5(c) for $r = 1$. Here the existence of the wavenumbers $q_2$ and $q_3$ as a function of $v$ can be seen and they appear when $v \in V_{II} = (0.815, 0.985)$.

The sets $V_I$ and $V_{II}$ have a particular physical interpretation. If $v \in V_I$, then no wave will be transmitted into the intact part of the structure. If $v \in V_{II}$, then one can find that waves will be transmitted inside the intact part of the structure. The dispersion diagrams (in Figs. 4 and 5) show that for certain $r$ values we can expect to encounter two different physical behaviours of the structure for quite large speeds $v$, by the presence of both speed ranges $V_I$ and $V_{II}$.

In Fig. 5(b), another property of the set $V_{II}$ is also highlighted, where the set can be composed of discrete intervals of values for $v$. Here, in Fig. 5(b), there occurs two small discrete intervals and for this value of $r$, $V_{II} = (0.74, 0.775) \cup (1.272, 1.3)$. The same behaviour of the set $V_I$ can also be asserted, and we refer to Fig. 5(a),

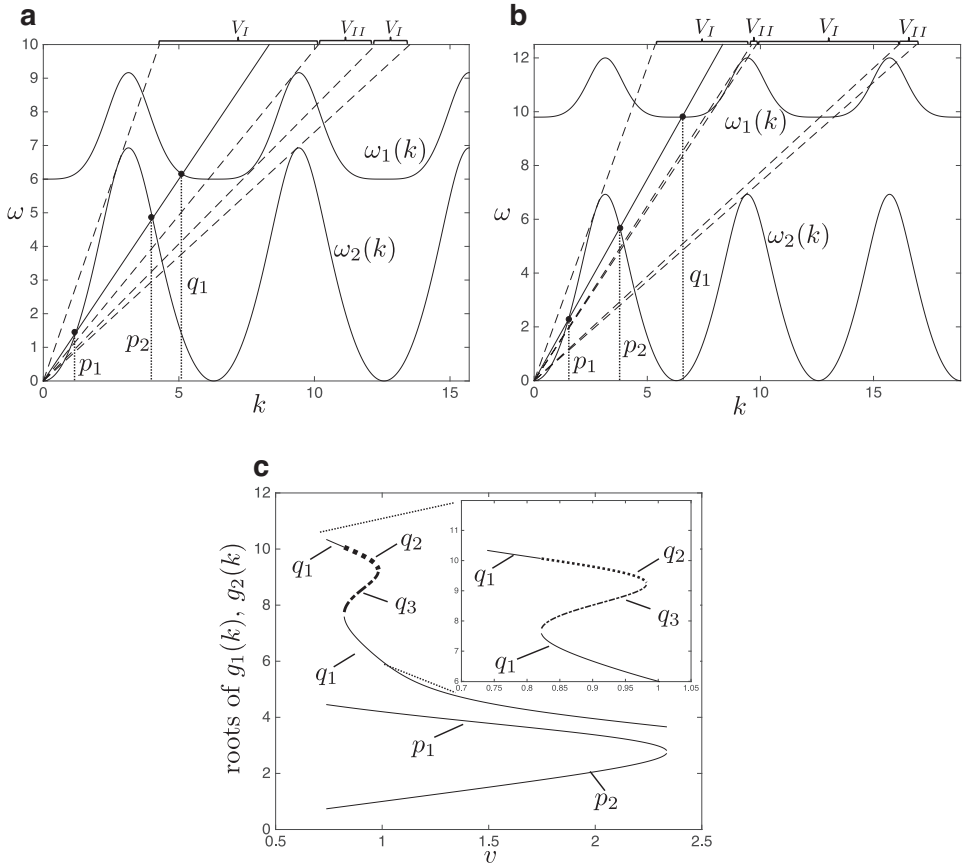


**Fig. 5.** (a) Dispersion relations $\omega_j(k)$, $j = 1, 2$, plotted as functions of the dimensionless wavenumber $k$, when $r = 1.5$. The line $\omega = kv$, for $v = v_1, 0.815, 0.985, 1.2$ and $v_2$, is presented. The description of $p_i$, $i = 1, 2$, and $q_j$, $1 \le j \le 3$ is given in Fig. 4. (b) Dispersion curves corresponding to the case when contrast parameter $r = 4$ and the lines $\omega = kv$ for $v = v_1, 0.775, 1.272, 1.3, 1.5$ and $v_2$. (c) The roots $p_i$, $i = 1, 2$, and $q_j$, $1 \le j \le 3$ plotted as functions of the dimensionless speed $v$ for $r = 1.5$.

to demonstrate that this set can be composed of two discrete intervals, represented as $V_I = (0.74, 0.815) \cup (0.985, 2.335)$. Therefore, for increasing $v$ inside $v_1 \le v \le v_2$, we may oscillate between either of the two physical regimes connected with the sets $V_I$ and $V_{II}$, (see Fig. 5(b)).

*3.2.3. General description of zeros of the functions* $g_j$, $j = 1, 2$

The function $g_2(k)$ has a double zero at $k = 0$ and two or more pairs of non-trivial simple zeros at $k = \pm p_1, \ldots, \pm p_{2n}$, where $n \ge 1$. Here $p_1 < p_2 < \cdots < p_{2n}$. Note that $n = 1$ when $v_1 < v < v_2$, whereas $n = 0$ for $v > v_2$ and non-trivial zeros of $g_2(k)$ do not exist.

For $j = 1, \ldots, n$

(i) at $k = p_{2j-1}$, $v < v_g$,

(ii) at $k = p_{2j}$, $v > v_g$,

as demonstrated in Fig. 4.

The function $g_1(k)$ has one, three or more pairs of simple zeros $k = \pm q_1, \ldots, \pm q_{2\nu+1}$, with $\nu \ge 0$. These zeros form a monotonically increasing sequence i.e. $q_1 < q_2 < \cdots < q_{2\nu+1}$. For each value of the contrast parameter $r$

$$\nu = 0, \quad \text{if} \quad v > v_0(r),$$

where $v_0(r)$ is a monotonically increasing function of $r$. As an example $v_0(r) \approx 1.0519$ when $r = 2$. Also note if $r \ge 2$

$$p_{2n} < q_1.$$

The preceding inequality does not hold if $r < 2$. For

(i) $j = 0, \ldots, \nu$, at $k = q_{2j+1}$, $v > v_g$,

(ii) $j = 1, \ldots, \nu$, at $k = q_{2j}$, $v < v_g$.

Here, those points corresponding to the inequality $v < v_g$, $(v > v_g)$ are located in the lower (upper) half of the complex plane after introduction of the small parameter $\varepsilon$ in the above problem (with $\varepsilon \to +0$).

In the next section we derive the general solution for the Wiener–Hopf equation for any speed $v$.

## 4. General solution of the Wiener–Hopf equation (22)

We discussed the waves propagating internally through two different parts of the structure, but these waves should be generated by an external action. Clearly, the collection of dynamic features inside the structure will depend on such an action. As an external load, here, we will define the remote force that produces waves propagating from infinity to the right inside the broken part of the structure (feeding waves), that will move the transition front to the right with a constant speed. This movement will initiate other waves (reflected waves that move from the right to the left and transmitted waves that move from the left to right of the transition front, see Slepyan, 2002).

We begin by rewriting the homogeneous equation (22) as

$$w_+(k) + L^*(k) w_-(k) = 0, \tag{28}$$

with $L^*(k) = g_2(k)/g_1(k)$, that has zeros and singular points located in both the upper and lower half of the complex plane and $L(k) \to 1$ as $k \to \pm\infty$. It is possible to construct $L^*$ in the form

$$L^*(k) = \frac{\Psi_+(k)}{\Psi_-(k)} L(k), \tag{29}$$

where according to Section 3.2.3

$$\Psi_+ = \frac{(1-\mathrm{i}k)^{2(\nu-n)}\prod_{j=1}^{n}(0-\mathrm{i}(k-p_{2j-1}))(0-\mathrm{i}(k+p_{2j-1}))}{\prod_{j=1}^{\nu}(0-\mathrm{i}(k-q_{2j}))(0-\mathrm{i}(k+q_{2j}))}, \tag{30}$$

$$\Psi_- = \frac{\prod_{j=0}^{\nu}(0+\mathrm{i}(k-q_{2j+1}))(0+\mathrm{i}(k+q_{2j+1}))}{(1+\mathrm{i}k)^{2(\nu-n)}(0+\mathrm{i}k)^2\prod_{j=1}^{n}(0+\mathrm{i}(k-p_{2j}))(0+\mathrm{i}(k+p_{2j}))}. \tag{31}$$

The meromorphic functions $\Psi_\pm$ admit the asymptotes

$$\Psi_\pm = 1 \pm \frac{2\mathrm{i}(\nu-n)}{k} + O\left(\frac{1}{k^2}\right), \quad k \to \pm\infty. \tag{32}$$

Note $L(k)$, has neither zeros nor singular points on the real axis. In addition, $L(k) > 0\ (-\infty < k < \infty)$ and $L(k) \to 1\ (k \to \pm\infty)$, with

$$\mathrm{Re}(L(\xi)) = \mathrm{Re}(L(-\xi)) \quad \text{and} \quad \mathrm{Im}(L(\xi)) = -\mathrm{Im}(L(-\xi)). \tag{33}$$

Thus, we may factorize it using the Cauchy type integral

$$L(k) = L_+(k)L_-(k),$$
$$L_\pm(k) = \exp\left[\pm\frac{1}{2\pi\mathrm{i}}\int_{-\infty}^{\infty}\frac{\ln L(\xi)}{\xi-k}\,\mathrm{d}\xi\right] \quad (\pm\Im k > 0) \tag{34}$$

with $L_\pm(\pm\mathrm{i}\infty) = 1$. The asymptotes for $L_\pm$ for $k \to \pm\infty$ are

$$L_\pm(k) = 1 \pm \frac{\mathrm{i}l_1}{k} + O\left(\frac{1}{k^2}\right), \quad \text{for } k \to \pm\infty. \tag{35}$$

with

$$l_1 = \frac{1}{2\pi}\int_{-\infty}^{\infty}\ln L(\xi)d\xi = \frac{1}{\pi}\int_0^{\infty}\ln|L(\xi)|d\xi. \tag{36}$$

Then (28) and (29) imply

$$\frac{1}{L_+(k)\Psi_+(k)}w_+(k) + \frac{L_-(k)}{\Psi_-(k)}w_-(k) = \Phi(k), \tag{37}$$

where $\Phi(k)$ represents the loading from the left of the transition front and appears as a result of the division through Eq. (28) by factors corresponding to zeros at $k = \pm p_{2j-1} - \mathrm{i}0,\ j = 1,\ldots,n$. The functions with the supports at $k = \pm p_{2j-1},\ 1 \le j \le n$, reflect the remote actions at the left. If this action has frequency $\omega = p_\nu v$, then this allows us to introduce in the right-hand side delta functions of $k$ at $\pm p_\nu$. Thus $\Phi(k)$ can take the form

$$\Phi(k) = \frac{C\mathrm{e}^{\mathrm{i}\phi}}{0+\mathrm{i}(k-p_\nu)} + \frac{C\mathrm{e}^{\mathrm{i}\phi}}{0-\mathrm{i}(k-p_\nu)} + \frac{\overline{C}\mathrm{e}^{-\mathrm{i}\phi}}{0+\mathrm{i}(k+p_\nu)} + \frac{\overline{C}\mathrm{e}^{-\mathrm{i}\phi}}{0-\mathrm{i}(k+p_\nu)}, \tag{38}$$

where $C$ is a complex constant to be determined and $\phi$ is the phase shift of the considered load.

The solution of the Wiener–Hopf equation (37) then follows as

$$w_+(k) = \Psi_+(k)L_+(k)\left[\frac{C\mathrm{e}^{\mathrm{i}\phi}}{0-\mathrm{i}(k-p_\nu)} + \frac{\overline{C}\mathrm{e}^{-\mathrm{i}\phi}}{0-\mathrm{i}(k+p_\nu)}\right] \tag{39}$$

and

$$w_-(k) = \frac{\Psi_-(k)}{L_-(k)}\left[\frac{C\mathrm{e}^{\mathrm{i}\phi}}{0+\mathrm{i}(k-p_\nu)} + \frac{\overline{C}\mathrm{e}^{-\mathrm{i}\phi}}{0+\mathrm{i}(k+p_\nu)}\right]. \tag{40}$$

### 4.1. Far-field behaviour of the structure

The poles of the functions $w_\pm$ reveal information about the dynamic features within the structure to the far left and right of the transition front. We now trace the expressions which determine the behaviour of the structure far away from the transition front.

For $\eta \to -\infty$, the behaviour of the original function $w$ can be identified in the form

$$w(\eta) \sim w_f + w_s + \sum_{j=1}^{n} w_r^{(j)}, \quad \eta \to -\infty. \tag{41}$$

Here the term $w_f$ corresponds to the feeding wave generated inside the structure which propagates to the transition front, that is determined by the poles $k = \pm p_\nu$ of $w_-$. Note the points $k = \pm p_\nu$ are removable singularities of $w_+$ defined by (39) and (30).

We assume that this feeding wave takes the form

$$w_f(\eta) = A\cos(p_\nu\eta - \phi), \tag{42}$$

where $A$ is the amplitude and $\phi$ is phase of this wave (already introduced in (37)–(40)). This feeding wave is produced from the load applied at $\eta = -\infty$. The phase shift, $\phi$ in (42) defines the position of the transition front, $\eta = 0$, relative to the wave (see (38)).

The functions $w_r^{(j)},\ 1 \le j \le n$, represent reflected waves propagating away from the transition front, associated with the poles $k = \pm p_{2j},\ 1 \le j \le n$. The term $w_s$ is a linear function of $\eta$ that represents the slope of the beam for $\eta \to -\infty$, which arises owing to the pole $k = 0$ of $w_-$ in (40).

It is worth noting that no wave will propagate inside the intact structure if $w_+$ has no poles along the real axis (see (30) and (39), for the case when $\nu = 0$). On the other hand, if $\nu \ge 1$, we can expect the transmission of feeding wave energy into the intact region and we find

$$w(\eta) \sim \sum_{j=1}^{\nu} w_{tr}^{(j)}, \quad \eta \to \infty, \tag{43}$$

where $w_{tr}^{(j)},\ 1 \le j \le \nu$, represent waves transmitted into the intact part of the structure. These transmitted waves correspond to the poles $k = \pm q_{2j},\ 1 \le j \le \nu$ of the function $w_+$.

Through an appropriate choice of $C$ in (39) and (40), a relation connecting $w_c$, $A$ and $\phi$ can be determined which governs the existence of the steady-state propagation of the transition front. The form of remaining functions $w_r^{(i)},\ 1 \le i \le n$, $w_t^{(j)},\ 1 \le j \le \nu$ and $w_s$ for $\eta \to -\infty$ can be determined explicitly using a similar approach.

In order to trace the expression for the feeding wave (42) from the asymptotes of $w_-$ in the vicinity of $k = \pm p_\nu$ it is necessary to choose $C$ in the right-hand side of (38) as:

$$C = \frac{L_-(p_\nu)}{\Psi_-(p_\nu)}\frac{A}{2a}, \tag{44}$$

and the detailed derivation of (44) can be found in Appendix A.

It also follows from (39) and (40) that

$$\frac{w(0)}{a} = \lim_{k\to\mathrm{i}\infty}(-\mathrm{i}k)w_+ = \lim_{k\to-\mathrm{i}\infty}(\mathrm{i}k)w_- = 2\mathrm{Re}(C\mathrm{e}^{\mathrm{i}\phi}), \tag{45}$$

and equating this to the critical displacement, $w_c$, we receive the first equation with respect to the unknown constants

$$2\mathrm{Re}(C\mathrm{e}^{\mathrm{i}\phi}) = \frac{w_c}{a}. \tag{46}$$

Here the division by $a$ appears as a result of the normalisation of displacement by the beam length in Section 3. Thus, $w_c$ is completely determined if the feeding wave amplitude and phase are supplied. Alternatively, (46) takes the form:

$$\cos(\phi + \psi_c) = \frac{|\Psi_-(p_\nu)|}{|L_-(p_\nu)|}\frac{w_c}{A}, \tag{47}$$

$$\psi_c = \arg(C) = \arg\left(\frac{L_-(p_\nu)}{\Psi_-(p_\nu)}\right). \tag{48}$$

It can then be established from (46) that the feeding wave amplitude $A$ and critical displacement $w_c$ must be chosen to satisfy

$$\frac{A}{w_c} \ge \Xi = \frac{|\Psi_-(p_\nu)|}{|L_-(p_\nu)|} \tag{49}$$

in order for the transition front to propagate steadily through the structure.

Owing to (32)–(36) the asymptote for $w_+$ in (39) as $k \to \pm\infty$ is

$$w_+(k) = \frac{2\mathrm{Re}(Ce^{i\phi})i}{k} - 2[\mathrm{Re}(Ce^{i\phi})\{l_1 + 2(v-n)\} + p_v \mathrm{Im}(Ce^{i\phi})]\frac{1}{k^2} + O\left(\frac{1}{k^3}\right). \quad (50)$$

Upon using the identity:

$$\lim_{\Im k \to +0} \int_0^\infty \eta^\lambda e^{ik\eta} d\eta = \frac{\Gamma(\lambda+1)}{(0-ik)^{\lambda+1}},$$

we obtain from (50) that

$$w(\eta) = w(+0) + \eta w'(+0) + O(\eta^2), \quad \text{for} \quad \eta \to +0,$$

where

$$w(+0) = 2a\,\mathrm{Re}(Ce^{i\phi})$$

and

$$w'(+0) = 2a\left[\mathrm{Re}(Ce^{i\phi})\{l_1 + 2(v-n)\} + p_v \mathrm{Im}(Ce^{i\phi})\right]. \quad (51)$$

Therefore, in accordance with (17), with (51) we prescribe that

$$\mathrm{Re}(Ce^{i\phi})\{l_1 + 2(v-n)\} + p_v \mathrm{Im}(Ce^{i\phi}) < 0, \quad (52)$$

where $C$ is determined by (44). The two conditions (46) and (52) are then necessary and sufficient for the transition front to propagate steadily through the structure.

#### 4.1.1. Minimum value of the feeding wave amplitude to steadily propagate the front with a given speed $v$

The function $\Xi$ in (49) defines the minimum value of the feeding wave amplitude that generates steady-state fracture at a given speed $v$. The function $\Xi$ and its dependence on $v$ for $v_1 \le v \le v_2$, is presented in Fig. 6(a), for various values of the contrast parameter $r$. The function is monotonically increasing for fixed $v$ and increasing $r$. Note that the dashed part of the curves correspond to those speeds $v \in V_{II}$. The function $\Xi$ is continuous as we move between the sets $V_I$ and $V_{II}$ for increasing $v$, and shows a singular behaviour as $v \to v_2$, (in this case $p_1$ and $p_2$ are approaching one another to form a resonance point and where this occurs $v = v_g$). The function $\Xi$ can change rapidly as we pass from $v \in V_I$ to $v \in V_{II}$ as shown for $r = 2$ in Fig. 6(a) near $v = 0.8$.

Fig. 6 (a) also shows the behaviour of the set $V_{II}$. The position of set $V_{II}$ shifts along the interval $v_1 \le v \le v_2$ and can redistribute into several discrete sets inside this interval, for increasing $r$. From $r = 1$ up to $r = 5.5$ one can identify an interval that forms part of the set $V_{II}$ that shrinks with increase of $r$, reducing the possibilities for transmission of waves into the intact structure. Further, for $r = 5.5$ we can see the appearance of another range of speeds for which transmitted waves can occur in the intact structure. Here, we refer to the representation of $V_{II}$ in terms of discrete intervals (mentioned in Section 3.2.2) in Fig. 6(a) that form the set $V_{II}$. The set $V_I$ also appears in Fig. 6(a) as the union of discrete intervals for $r > 1$.

A plot of the ratio $A/w_c$ as a function of the feeding wave speed is provided in Fig. 6(b) for the case $r = 1$ and various speeds $v$. Note that condition (49) indicates the range of values for $\phi$ for which (46) is valid and this range also depends on the speed of the transition front. In addition, the right-hand side in (47) is positive and only values of $\phi$ for which this condition is valid should be accepted if the feeding wave amplitude and the critical displacement are known.

In Fig. 6(b), we see that the range of $\phi$ for which (47) is valid shifts in the positive direction along the horizontal axis for increasing $v$. For a given value of $v$, the curve will approach two vertical asymptotes for values that coincide with the upper and lower bounds of the range of admissible $\phi$ values.

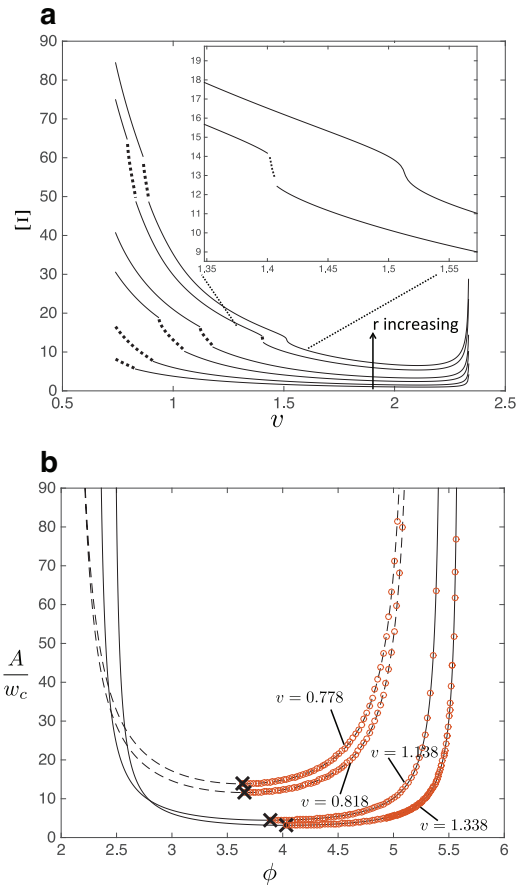


**Fig. 6.** (a) The dependence of $\Xi$ on the dimensionless speed $v$ for $r = 0.5, 1, 2, 3, 5.5$ and 6. Dashed parts of each curve correspond to speeds $v \in V_{II}$ for that particular $r$ value. (b) The ratio $A/w_c$ plotted as a function of the phase $\phi$, for $r = 1$ and several values of the dimensionless speed. Dashed lines indicate the results for those speeds in the set $V_{II}$. The minimum for each curve is marked with a cross, which correspond to the points $(\phi, A/w_c) = (4.033, 3.161)$, $(3.884, 4.471)$, $(3.656, 11.589)$ and $(3.634, 13.836)$. These points coincide with the value of $\Xi$ for the given values of $v$. In addition, circles have been added to curve to indicate combinations of $\phi$ and $A/w_c$ for which (52) is invalid.

For every value of the transition front speed $v$, there is a value of $\phi$ for which the ratio $A/w_c$ takes its minimum value. Physically, for a given $w_c$, these points can be linked to the minimum amplitude $A$ of the feeding wave required to propagate the transition front with a constant speed. It also implies that the energy generated by feeding wave to create the latter scenario is also at a minimum (see Section 5). For every value of $A/w_c$ above this minimum value, we see there corresponds two values of $\phi$ satisfying condition (46).

We indicate on the curves in Fig. 6(b) those values of $A/w_c$ and $\phi$ for which condition (52) is not satisfied. For all speeds we show that the choice of $\phi$ is unique, and this is taken from the left of the minimum point of each curve.

### 4.2. Other dynamic features to the left of the transition front

#### 4.2.1. The reflected waves

The terms $w_r^{(j)}$, $1 \le j \le n$, correspond to the reflected waves (produced by poles at $k = \pm p_{2j} + i0$ of $w_-$ in (40)). They can also be derived through application of the residue theorem and the inverse Fourier transform. The function $w_r^{(j)}$, $1 \le j \le n$, takes the form

$$w_r^{(j)}(\eta) = A_r^{(j)} \cos(p_{2j}\eta - \psi_r^{(j)} - \alpha_r^{(j)}), \quad \text{for} \quad 1 \le j \le n, \quad (53)$$

where the reflected wave amplitude is given as

$$A_r^{(j)} = \frac{4a|\Psi_-^r(p_{2j})||C|}{|p_{2j}^2 - p_\nu^2||L_-(p_{2j})|} \times \sqrt{(p_{2j}\cos(\phi+\psi_c))^2 + (p_\nu \sin(\phi+\psi_c))^2}, \quad (54)$$

and

$$\Psi_-^r(p_{2j}) = \lim_{k\to p_{2j}} (0 + \mathrm{i}(k - p_{2j}))\Psi_-(k).$$

The terms in this wave's phase shift are

$$\psi_r^{(j)} = \arg\left(\frac{\Psi_-^r(p_{2j})}{\mathrm{i}L_-(p_{2j})}\right) \quad (55)$$

and

$$\alpha_r^{(j)} = \arg\left(\frac{1}{p_{2j}^2 - p_\nu^2}\{p_{2j}\cos(\phi+\psi_c) + \mathrm{i}p_\nu \sin(\phi+\psi_c)\}\right),$$
$$\psi_c = \arg(C). \quad (56)$$

For a detailed discussion of the derivation of the functions $w_r^{(j)}$, $1 \le j \le n$, see Appendix A.

#### 4.2.2. The inclination of the beam to the far left of the transition front

The remaining second order pole of $w_-$, at $k = 0\mathrm{i}$, in (40) gives us the expression for the slope of the beam when $\eta \to -\infty$. The inclination of the beam to the far left of the transition front takes the form

$$w_s(\eta) = A_s\eta + B_s \quad (57)$$

where the coefficient of the linear term in $\eta$ is

$$A_s = \frac{2a\,\mathrm{Im}(Ce^{\mathrm{i}\phi})\Psi_-^{sl}(0)}{p_\nu L_-(0)} \quad (58)$$

and the constant

$$B_s = \frac{2a\,\mathrm{i}\mathrm{Im}(Ce^{\mathrm{i}\phi})(\Psi_-^{sl})'(0)}{p_\nu L_-(0)} + \frac{2a\Psi_-^{sl}(0)}{p_\nu L_-(0)}\left[\frac{\mathrm{Re}(Ce^{\mathrm{i}\phi})}{p_\nu} + \frac{\mathrm{Im}(L_-'(0))}{L_-(0)}\mathrm{Im}(Ce^{\mathrm{i}\phi})\right]. \quad (59)$$

Here, $C$ is defined in (44) and

$$\Psi_-^{sl}(k) = \frac{(-1)^{\nu-n+1}\prod_{j=0}^{\nu}(k^2 - q_{2j+1}^2)}{(1+\mathrm{i}k)^{2(\nu-n)}\prod_{j=1}^{n}(k^2 - p_{2j}^2)}. \quad (60)$$

### 4.3. Dynamic features to the right of the transition front

#### 4.3.1. The transmitted waves $w_{tr}^{(j)}$

In addition to the reflected waves propagating inside the structure to the left of the transition front (see Section 4.2.1), for $\nu > 0$ there exist transmitted waves inside the intact structure. The form of these waves can be traced by considering the poles at $k = \pm q_{2j} - \mathrm{i}0$, $1 \le j \le \nu$, in the function $w_+$ (see (39)). Therefore, when $\nu$ is chosen so that $\nu > 0$ and $\eta \to \infty$, one will see a linear combination of the waves $w_{tr}^{(j)}$, $1 \le j \le \nu$, in accordance with (43), where

$$w_{tr}^{(j)}(\eta) = A_{tr}^{(j)}\cos(q_{2j}\eta - \psi_{tr}^{(j)} - \alpha_{tr}^{(j)}), \quad 1 \le j \le \nu. \quad (61)$$

Here

$$A_{tr}^{(j)} = \frac{4a|\Psi_+^{tr}(q_{2j})||C||L_+(q_{2j})|}{|q_{2j}^2 - p_\nu^2|} \times \sqrt{(q_{2j}\cos(\phi+\psi_c))^2 + (p_\nu\sin(\phi+\psi_c))^2} \quad (62)$$

where

$$\Psi_+^{tr}(q_{2j}) = \lim_{k\to q_{2j}} (0 - \mathrm{i}(k - q_{2j}))\Psi_+(k),$$

and terms in the phase of these waves are

$$\psi_{tr}^{(j)} = \arg(\mathrm{i}\Psi_+^{tr}(q_{2j})L_+(q_{2j})),$$
$$\alpha_{tr}^{(j)} = \arg\left(\frac{1}{q_{2j}^2 - p_\nu^2}\{q_{2j}\cos(\phi+\psi_c) + \mathrm{i}p_\nu\sin(\phi+\psi_c)\}\right), \quad (63)$$

with $\psi_c$ defined in (48). Note that the functions $w_t^{(j)} = 0$, $1 \le j \le \nu$ if $\nu \in V_I$ (this case corresponds to $\nu = 0$).

### 4.4. The rotation of each mass inside the structure

Having established the behaviour of the structure far from the transition front we now use the results of the previous sections to address the behaviour of the rotations by using (19).

#### 4.4.1. Rotations of the masses to the left of the transition front produced by the waves and the inclination

Using the (42) and results of Section 4.2.1, the forms of the waves that exist inside the damaged part of structure are

$$w_f(\eta) = A\cos(p_\nu\eta - \phi), \quad (64)$$

$$w_r^{(j)}(\eta) = A_r^{(j)}\cos(p_{2j}\eta - \psi_r^{(j)} - \alpha_r^{(j)}), \quad (65)$$

with $1 \le j \le n$. We will concentrate on the feeding wave $w_f(\eta)$ as in what follows results for the reflected (and transmitted waves in the next section) can be derived in a similar way.

The Fourier transform of $w_f(\eta)$ is then

$$w_f^{\mathrm{F}} = = \pi A\left[e^{\mathrm{i}\phi}\delta(k - p_\nu) + e^{-\mathrm{i}\phi}\delta(k + p_\nu)\right]. \quad (66)$$

Insertion of this in (19) gives an expression for the Fourier transform of rotations $\theta_f^x$ generated by the feeding wave:

$$\theta_f^{x\mathrm{F}} = -\frac{3\pi\,\mathrm{i}\sin k}{a(2+\cos k)}A[e^{\mathrm{i}\phi}\delta(k - p_\nu) + e^{-\mathrm{i}\phi}\delta(k + p_\nu)]. \quad (67)$$

Applying the inverse Fourier transform yields

$$\theta_f^x(\eta) = -\frac{3A\mathrm{i}}{2a}\frac{\sin p_\nu}{(2+\cos p_\nu)}[e^{-\mathrm{i}(p_\nu\eta-\phi)} - e^{\mathrm{i}(p_\nu\eta-\phi)}]. \quad (68)$$

Therefore,

$$\theta_f^x(\eta) = -3A\frac{\sin p_\nu}{a(2+\cos p_\nu)}\sin(p_\nu\eta - \phi). \quad (69)$$

In a similar way to (64) and (66)–(68), we can derive expressions for the rotations $\theta_r^{x,j}$ associated with reflected waves $w_r^{(j)}$, in (65), as

$$\theta_r^{x,j}(\eta) = -3A_r^{(j)}\frac{\sin p_{2j}}{a(2+\cos p_{2j})}\sin(p_{2j}\eta - \psi_r^{(j)} - \alpha_r^{(j)}),$$

for $1 \le j \le n$.

In addition to the feeding and reflected waves existing to the left of the transition front, in Section 4.2.2, we also showed there exists a slope behind the transition front. To calculate the rotations produced by the slope, we take the Fourier transform of (57) to obtain

$$w_s^{\mathrm{F}} = 2\pi[-\mathrm{i}A_s\delta'(k) + B_s\delta(k)]. \quad (70)$$

Then, in a similar way to the previous section, using (70) we can write

$$\theta_s^x(\eta) = \frac{A_s}{a}, \quad (71)$$

where $\theta_s^x$ are the rotations produced by the linear function $w_s$.

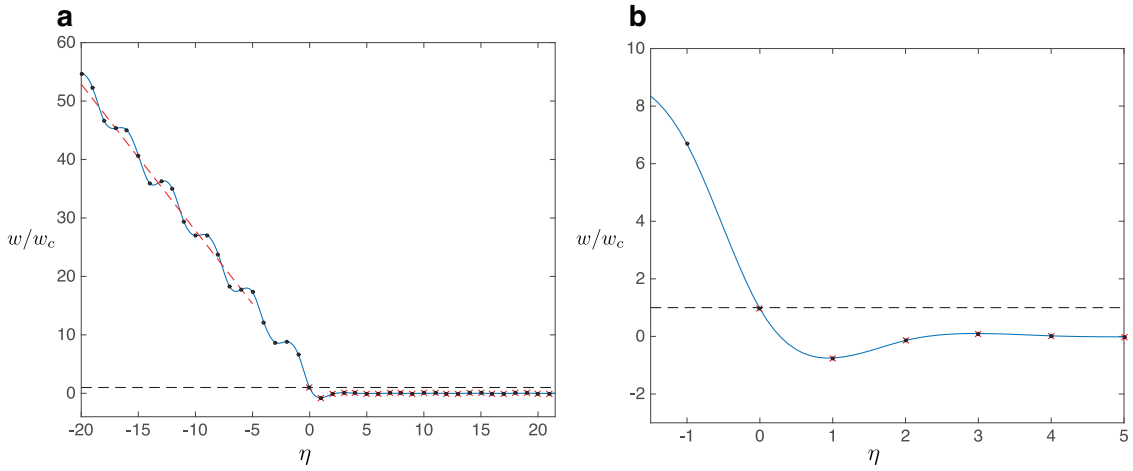


**Fig. 7.** Displacements along the central axis of the beam-made strip based on the inverse Fourier transform of (39), (40) and (19). Masses in the structure are shown by black dots and those masses which are supported by transverse links are also provided with red-crosses ($\eta \geq 0$). In (a), we show the displacements both ahead and behind the transition front, where one can observe the slope inside the structure and the feeding and reflected waves. The gradient of the slope (also predicted by the theory) is represented by the red dashed line, with gradient equal to $A_s(= -6.287)$ of (57). In (b), we show computations in the vicinity of the transition front, that shows no wave is transmitted to the intact structure. Parameters used in the computations where $M = 1$, $a = 1$, $E_1 = I_1 = 1$, $E_2 I_2 = 0.5$, ($r = 0.5$), and $w_c = 2.51$. The feeding wave amplitude is $A = 5.002$ and this profile occurs as the front steadily propagates with speed $v = 1.7214 \in V_I$. (For interpretation of the references to colour in this figure legend, the reader is referred to the web version of this article.)

*4.4.2. Rotations of the masses produced by the transmitted waves ahead of the front*

In similar way to the derivation of (69), we can assert that the rotations $\theta_{tr}^{x,j}$ produced by the waves $w_{tr}^{(j)}$, $1 \leq j \leq \nu$, (see (61)), are given by the formula

$$\theta_{tr}^{x,j}(\eta) = -3A_{tr}^{(j)} \frac{\sin q_{2j}}{a(2+\cos q_{2j})} \sin(q_{2j}\eta - \psi_{tr}^{(j)} - \alpha_{tr}^{(j)}).$$

*4.5. Illustration: beam profiles during the steady-state fracture process*

One can compute the inverse Fourier transform of (39) and (40) to retrieve the analytical solution for the displacements. In addition, the solution presented in (39) and (40) needs to be combined with (19), and then the inverse Fourier transform is taken to receive the rotations of each mass. The inverse Fourier transforms can be computed numerically to obtain values of the mass rotations and displacements and we can use these to construct the beam displacements between each node along the central axis of the structure with (4).

The results are shown for two cases, when $v \in V_I$ and $v \in V_{II}$ in Figs. 7 and 8, respectively. In Fig. 7(a), we show the normalised displacements $w/w_c$ along the central beam of the structure as a function of $\eta$ ahead and behind the transition front. In this case, nodes have mass $M = 1$ and the beams have the properties $a = 1$, $E_1 = I_1 = 1$, $E_2 I_2 = 0.5$, ($r = 0.5$), and $w_c = 2.51$. The feeding wave amplitude is $A = 5.002$. For these parameters, the speed of the transition front is $v = 1.7214 \in V_I$. Masses are represented in this figure by the black dots and those which are supported by the transverse beams are supplied with red crosses ($\eta \geq 0$). We also represent the critical displacement condition $w/w_c = 1$ by the horizontal dashed line. In Fig. 7(b), we present the same displacements in the vicinity of the transition front ($\eta = 0$).

During the steady-state fracture process, one can clearly identify the slope behind the transition front (in Fig. 7(a)), along which the feeding and reflected waves propagate along. The gradient of this slope is predicted using $A_s$ of (57), we also supply a red dashed line having gradient $A_s = -6.287$ demonstrating the slope behind the transition front has exactly this inclination. On the other hand, as $v \in V_I$, according to the theory presented here, no wave is transmitted to the intact structure and this is precisely what is observed in both Fig. 7(a) and (b).

On the contrary, when $v \in V_{II}$, one may expect the transmission of a wave into the intact structure. In Fig. 8(a), a view of the profile of the structure is given, for the same material parameters as in Fig. 7. Here, the feeding wave amplitude is $A = 8.077$, the inclination of the slope $A_s = -5.435$, the critical displacement $w_c = 0.5468$ and $v = 0.7745 \in V_{II}$. Again for $v \in V_{II}$ we see the slope following the propagation of the transition front. In Fig. 8, we demonstrate there is a wave transmitted into the intact structure with amplitude $A_t = 0.07672$ when $v \in V_{II}$ (clearly observed for $\eta > 2$ in Fig. 8(b), indicated by the red dashed line $A_t/w_c$), whereas near $\eta = 0$ there is also some local deformation near the transition front.

## 5. Energy redistribution within the structure

In this section we investigate how the energy carried by the feeding wave is distributed within in the structure during the fracture process. In particular, we identify how the slope occurring behind the transition front influences the wave radiation properties observed in the fracture process.

*5.1. Energy balance*

The energy $G_f$ carried by the feeding wave can be written as the sum of energies carried by the other waves inside the structure, in addition to the kinetic energy given to the masses by the linear deformation (57) and the strain energy required to break transverse links at $\eta = 0$. Thus, we can write

$$G_f = G_0 + \sum_{j=1}^{n} G_r^{(j)} + \sum_{j=1}^{\nu} G_{tr}^{(j)} + G_k \tag{72}$$

where

(i) $G_0$ is the energy spent on breaking the transverse links,
(ii) $G_r^{(j)}$, $1 \leq j \leq n$, is the energy carried by the reflected waves,
(iii) $G_{tr}^{(j)}$, $1 \leq j \leq \nu$, is that carried by the transmitted waves, and
(iv) $G_k$ is the kinetic energy of the masses generated by (57).

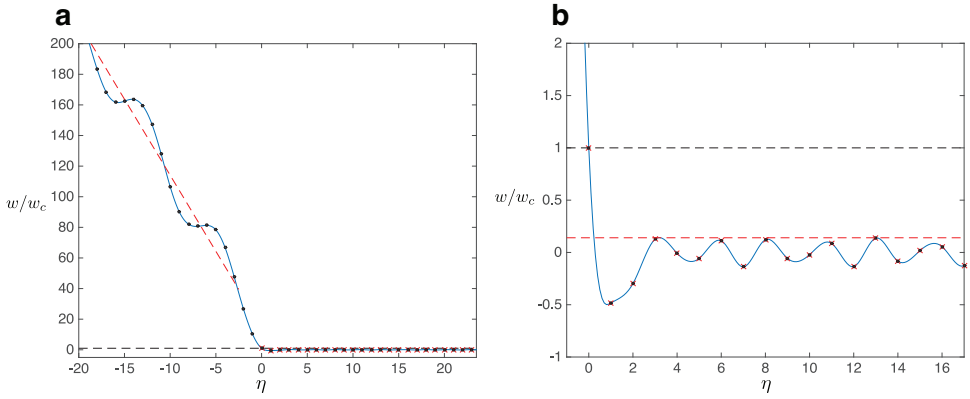


**Fig. 8.** Displacements along the central axis of the beam-made strip based on the inverse Fourier transform of (39), (40) and (19). Description of both diagrams is given in Fig. 7. In (a), again we show the slope inside the structure and the feeding and reflected waves during the fracture process. The gradient of the slope (also predicted by the theory) is represented by the red dashed line, with gradient equal to $A_s(=-5.435)$ in (57). In (b), we show computations in the vicinity of the transition front, where a wave is transmitted to the intact structure with amplitude $A_t = 0.07672$ (a red dashed line corresponding to $A_t/w_c$ is shown). Parameters used in the computations where $M = 1$, $a = 1$, $E_1 = I_1 = 1$, $E_2 I_2 = 0.5$, $(r = 0.5)$, and $w_c = 0.5468$. The feeding wave amplitude is $A = 8.077$ and this profile occurs as the front steadily propagates with speed $v = 0.7745 \in V_{II}$. (For interpretation of the references to colour in this figure legend, the reader is referred to the web version of this article.)

#### 5.1.1. The strain energy $G_0$

The energy released due to the breakage of the two transverse links at $\eta = 0$ can be computed as

$$G_0 = -\int_0^a \mathcal{M}(y,t)\frac{\partial^2 W(y,t)}{\partial y^2}dy = \frac{12E_2I_2}{a^3}w_c^2, \tag{73}$$

where it is noted that the quantity $W$ is defined by (7) for $\eta = 0$ (under the assumption $w_m(t) = w(\eta)$, $\theta_m^x(t) = \theta^x(\eta)$) and $\mathcal{M}$ is given in (5) with $E = E_2$ and $I = I_2$. Here, if the feeding wave amplitude $A$ and the phase $\phi$ are supplied, then $G_0$ can be calculated using (46) and (73).

#### 5.1.2. The energy carried by the feeding and dissipative waves

The energy $G_f$ carried by the feeding wave takes the form

$$G_f = aN_f\frac{|v_g - v|}{v_g}, \tag{74}$$

whereas the energies $G_r^{(j)}$ and $G_{tr}^{(j)}$ carried by the reflected and transmitted waves, respectively, can be calculated through

$$G_J^{(j)} = aN_J^{(j)}\frac{|v_g - v|}{v_g}, \quad J = r, tr. \tag{75}$$

Here $N_f$ is the time-averaged energy flux density produced by the feeding wave and this is given by

$$N_f = \frac{3A^2E_1I_1p_vV\sin(p_v)(\cos(p_v)+5)(1-\cos(p_v))}{a^4(2+\cos(p_v))^2} \tag{76}$$

and for the reflected and transmitted waves

$$N_J^{(j)} = \frac{3(A_J^{(j)})^2E_1I_1k_J^{(j)}V\sin(k_J^{(j)})(\cos(k_J^{(j)})+5)(1-\cos(k_J^{(j)}))}{a^4(2+\cos(k_J^{(j)}))^2},$$
$$J = r, \quad tr, \tag{77}$$

where

$$k_r^{(j)} = p_{2j}, \quad 1 \le j \le n, \quad \text{and} \quad k_{tr}^{(j)} = q_{2j}, \quad 1 \le j \le \nu.$$

Also, $v_g$ is the group velocity for the wave considered ($v_g = \frac{d\omega}{dk}$).

#### 5.1.3. Kinetic energy of the masses along the inclination of the beam

The kinetic energy for the masses along the inclination observed for $\eta \to -\infty$ is

$$G_k = \frac{M}{2}\left(\frac{\partial w_s(\eta)}{\partial t}\right)^2 = \frac{M}{2}\frac{V^2}{a^2}A_s^2, \tag{78}$$

which follows from (57).

### 5.2. Illustration: energy ratios

#### 5.2.1. Dependence of the energy ratios on $\phi$

In this section, we present numerical computations for the speed range $v_1 < v < v_2$, showing how the energy from the feeding wave is distributed within the structure during the fracture process. For this speed range, there exists a single reflected wave $((n = 1), G_r^{(j)} = G_r)$ in the structure and the existence of transmitted waves depends on the speed $v$ and the contrast parameter $r$. Also, as discussed in Section 3.2.2, this speed range may be partitioned into the two sets $V_I$ and $V_{II}$. For $v \in V_{II}$, $\nu = 1$ and there is a single transmitted wave in the intact structure. The energy this wave carries is denoted by $G_{tr}^{(j)} = G_{tr}$. If $v \in V_I$, then there exist no transmitted waves in the intact structure and in (72) the terms $G_{tr}^{(j)} = 0$, $1 \le j \le \nu$ (in fact in this case $\nu = 0$).

In Fig. 9(a) and (b), we show the dependence of the energy ratios $G_0/G_f$, $G_r/G_f$, $G_{tr}/G_f$ and $G_k/G_f$ (using (73)–(78)) on the phase shift $\phi$ for the contrast parameter $r = 1$. In this figure, it can be seen that in accordance with (72), the energy ratios sum to unity.

This figure shows some main features of the energy ratios as functions of $\phi$, which can be observed for any value of $r$. In particular, there exists an optimal value of $\phi = \phi^* = 2\pi - \psi_c$ for which the energy carried by the waves $G_r$, $G_{tr}$ inside the structure and the energy released due to fracture $G_0$ take their maximum value, e.g. in Fig. 9(a), this occurs for approximately $\phi = 3.6$.

At this optimal value of $\phi$, the kinetic energy $G_k$ within the structure is zero. Consulting (78), this implies the inclination $A_s$ of the structure to the far-left of the transition front is zero and therefore the feeding wave energy is distributed only amongst the waves. According to (71), it also means the rotations produced by (57) to the far-left of the front are equal to zero. Thus, in the case $\phi^* = 2\pi - \psi_c$, masses will rotate as a result of the influence of the waves inside the structure and no contribution to this rotation occurs as a consequence of the deformation (57) (which is constant).

The phase $\phi^* = 2\pi - \psi_c$ gives rise to the extremum in the energy ratios and corresponds to the minimum feeding wave energy required to propagate the transition front with a constant speed (see Section 4.1.1).

Fig. 9 also shows how the feeding wave energy is distributed for $v \in V_I$ and $v \in V_{II}$. For $v \in V_{II}$, we see the presence of a transmitted wave in the intact structure and thus some of the feeding wave energy is given to this wave in Fig. 9(a). Note that when $v \in V_I$, we no longer expect any transmission of waves into the intact structure (since $\nu = 0$), therefore the energy in this case goes to the

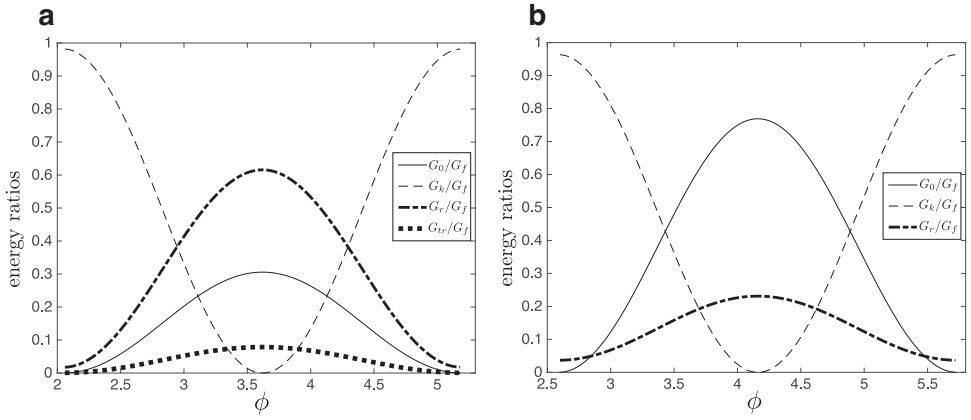


**Fig. 9.** The energy ratios $G_0/G_f$, $G_r/G_f$, $G_{tr}/G_f$ and $G_k/G_f$ plotted as functions of the phase $\phi$ for $r = 1$, and (a) $\nu = 0.75$ ($\nu \in V_{II}$) and (b) $\nu = 1.5$ ($\nu \in V_I$).

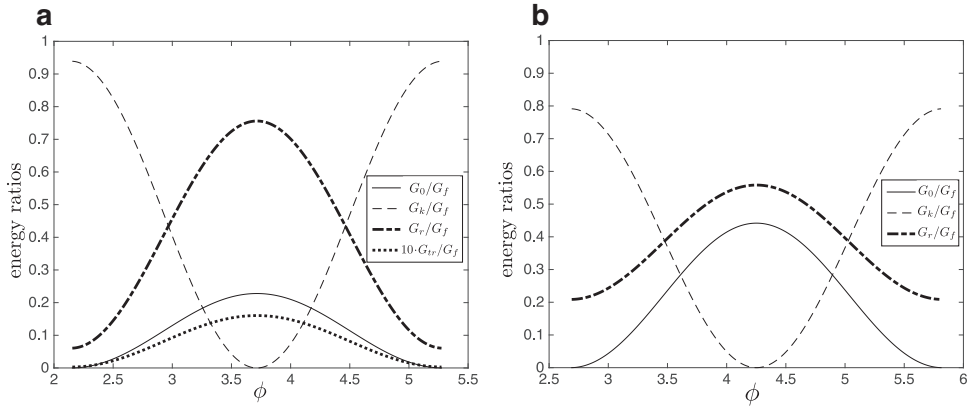


**Fig. 10.** The energy ratios $G_0/G_f$, $G_r/G_f$, $10 \cdot G_{tr}/G_f$ and $G_k/G_f$ plotted as functions of the phase $\phi$ for $r = 3$ and (a) $\nu = 1.15$ ($\nu \in V_{II}$) and (b) $\nu = 2$ ($\nu \in V_I$).

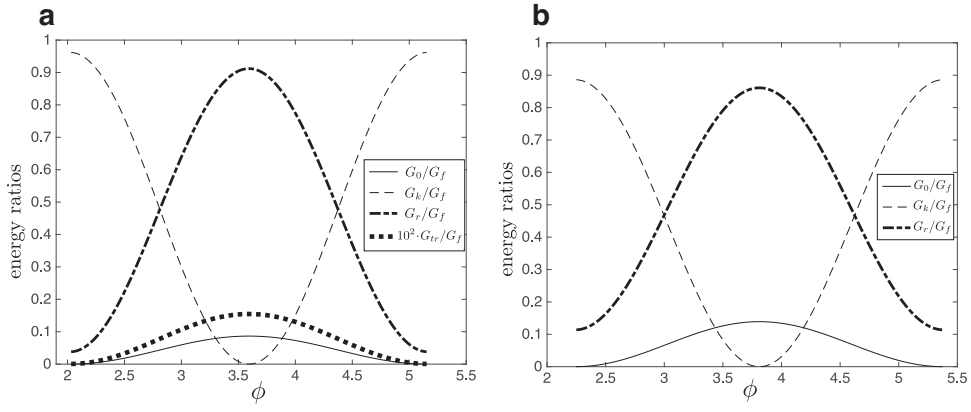


**Fig. 11.** The energy ratios $G_0/G_f$, $G_r/G_f$, $10^2 \cdot G_{tr}/G_f$ and $G_k/G_f$ plotted as functions of the phase $\phi$ for $r = 6$, and (a) $\nu = 0.88$ ($\nu \in V_{II}$) and (b) $\nu = 1.4$ ($\nu \in V_I$).

reflected waves and the slope of the broken part of the structure as in Fig. 9(b).

We also consider different values of the contrast parameter $r$ and its effect on the energy ratios. In particular, taking $r > 1$ we observe in Figs. 10 and 11 that the intact structure allows for less energy to be carried by the transmitted wave (and this part of the structure begins to act like a rigid interface with increase of $r$). In this case, more energy is spent on the reflection of the waves. In particular for increasing $r$, if $\nu \in V_{II}$, the energy carried by the transmitted wave in the intact structure is clearly seen to decrease quite rapidly for all $\phi$ (see Figs. 10(a) and 11(a)). For example, in the cases $r = 3$ and $r = 6$ in Figs. 10(a) and 11(a), respectively, the effect generated by the transmitted waves is very small. As a result, in these figures, the values of $G_{tr}/G_f$ have been appropriately scaled to demonstrate their effect on the partition of feeding wave energy. Here, large $r$ corresponds to the intact structure having stiffer transverse supports or a larger rotational inertia, due to either Young's modulus or the second moment of area being larger, in comparison to those properties for the horizontal links. Such a contrast in these material properties could influence the vibrations within the intact structure, making them smaller, and hence we see the decrease in the magnitude of $G_{tr}/G_f$ as we increase $r$.

For $r < 1$, we can expect much more energy of the feeding wave to be transmitted into the intact structure for $\nu \in V_{II}$ (see Fig. 12(a)). Note that the energy given to the transmitted waves in Figs. 10–12 is always less than the energy carried by the reflected

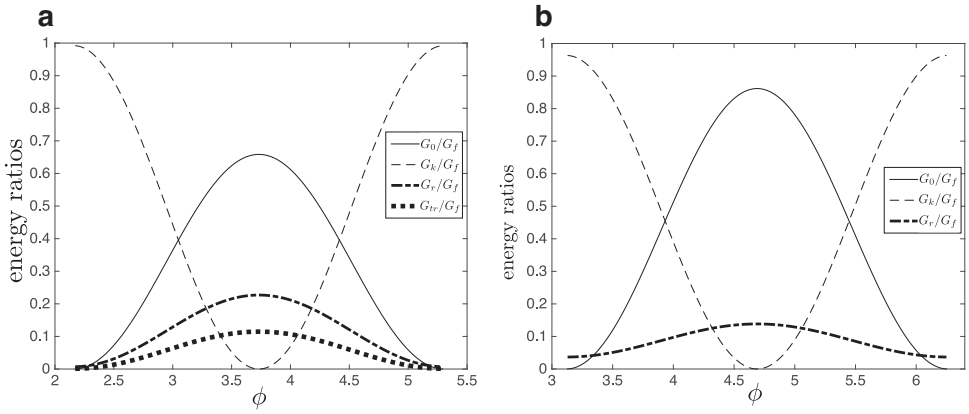


**Fig. 12.** The energy ratios $G_0/G_f$, $G_r/G_f$, $G_{tr}/G_f$ and $G_k/G_f$ plotted as functions of the phase $\phi$ for $r = 0.5$ (a) $v = 0.78$ ($v \in V_{II}$) and (b) $v = 1.8$ ($v \in V_I$).

waves. The energy spent on fracture is also seen to decrease as we increase $r$ in Figs. 10–12.

The way the energy is partitioned inside the structure is dependent on the feeding wave phase $\phi$. Focusing on Fig. 12(a), we observe for approximately $\phi \in [2.25, 3.1]$, most of the feeding wave energy is given to the slope behind the transition front, with the rest being distributed to the waves and the fracture energy. When $\phi$ increases inside the interval [3.1, 3.7] ($\psi_c = 3.7$), the energy along the slope tends to zero at $\psi = \psi_c$, whereas the energy distributed to the fracture process and the waves increases. Similar competition between the energy consumption of the dynamic features of the structure can be found in Figs. 10–12.

## 6. Conclusions

Here we have considered dynamic fracture inside a discrete structure composed of periodically placed masses connected by beams. This problem has been solved using the Wiener–Hopf technique (Noble, 1958) for any given speed $v$ of the transition front. Two distinct regimes of the structure have been identified during the steady-state fracture process for a specific range of the speed $v$. In one of these regimes, there exists a sinusoidal wave transmitted to the intact part of the structure. In the other regime, only the evanescent waves exists there.

We have also identified the magnitude of the feeding wave amplitude required to propagate the transition front with a constant speed $v$. One may also observe a rapid transition of the feeding wave energy associated with this amplitude as the structure moves between the regimes discussed above.

Note that the displacement criterion at the transition front is insufficient in guaranteeing the steady-state regime. In addition, it is necessary to prescribe that the displacement of nodes ahead of the transition front remain below this critical displacement (Marder and Gross, 1995). This admissibility criterion is violated when the feeding wave amplitude (at a given frequency) is high enough. In such cases, alternative ordered regimes arise (Mishuris et al., 2009a; Slepyan et al., 2015). Alternative regimes arising in the considered structure are examined separately.

In the analysis of the structural dynamics during fracture, we have identified that behind the transition front, waves reflected from and incident on the front will propagate along a slope. Ahead of the front, one may find waves transmitted to the intact structure. Rotations of the masses also accompany the displacements produced by these effects.

The distribution of energy amongst these dynamic effects has also been obtained. The minimum energy required to propagate the front steadily with a certain speed has been shown to coincide with the case when the gradient of the slope behind the front vanishes. Consequently, it occurs that the rotations for the masses associated with this inclination are zero, and there only one can expect the rotations of these masses to be produced by the feeding and reflected waves.

## Acknowledgement

The authors gratefully acknowledge the financial support of the European Seventh Framework Programme under Contract nos. PIAP-GA-2012-284544-PARM2.

## Appendix A

First, we provide the details of the derivations of (44) and (49) in Section A.1, where the latter determines the lower bound for the feeding wave energy required to propagate the transition front with constant speed. Then in Section A.2, we determine the dynamic features of the structure during the fracture process.

### A.1. Derivation of (44)

For a large distance from the transition point, the feeding wave is also defined by the residue at $k = \pm p_v + \mathrm{i}0$ in the inverse Fourier transform. From (40), the leading order term in the function defining $w_-$ at $k = p_v$ is

$$\frac{\Psi_-(p_v)}{L_-(p_v)} \frac{Ce^{\mathrm{i}\phi}}{0 + \mathrm{i}(k - p_v)}, \tag{A.1}$$

and for $k \to -p_v$ it is

$$\frac{\overline{\Psi_-(p_v)}}{\overline{L_-(p_v)}} \frac{\overline{C}e^{-\mathrm{i}\phi}}{0 + \mathrm{i}(k + p_v)}.$$

Here $\Psi_-(p_v)$ of (31) is simplified to

$$\Psi_-(p_v) = (-1)^{v-n} \frac{1}{p_v^2} \frac{\prod_{j=0}^{v}(p_v^2 - q_{2j+1}^2)}{\prod_{l=1}^{n}(p_v^2 - p_{2j}^2)} (1 + \mathrm{i}p_v)^{2(n-v)},$$

and owing to (30), (31) and (33),

$$L_-(-k) = \overline{L_-(k)},$$
$$\Psi_\pm(-k) = \overline{\Psi_\pm(k)}.$$

Therefore, choosing $C$ as in (44) and applying the residue theorem at the poles $k = \pm p_v + 0\mathrm{i}$ of $w_-$, for $\eta \to -\infty$ we receive (42) as the expression for the feeding wave (here $a$ again appears because of the normalisation of $w$ by the beam length in Section 3).

*A.2. Derivation of dynamic features of the beam structure*

*A.2.1. Derivation of the expressions for the reflected waves $w_r^{(j)}$.* Now we show how to obtain the representation for the reflected waves $w_r^{(j)}$, $1 \le j \le n$ in Section 4.2.1. The function $w_r^{(j)}$ arises in the consideration of the residues of $k = \pm p_{2j} + 0\mathrm{i}$ in the expression for $w_-$ in (40). The leading order term in asymptotics of the function defining $w_-$ in (40), for $k \to \pm p_{2j}$ is

$$\frac{\Psi_-^r(\pm p_{2j})}{\mathrm{i}L_-(\pm p_{2j})}\left[\frac{C e^{\mathrm{i}\phi}}{(\pm p_{2j} - p_\nu)} + \frac{\overline{C} e^{-\mathrm{i}\phi}}{(\pm p_{2j} + p_\nu)}\right]\frac{1}{0 + \mathrm{i}(k \mp p_{2j})},$$

where

$$\Psi_-^r(\pm p_{2j}) = \lim_{k \to \pm p_{2j}} (0 + \mathrm{i}(k \mp p_{2j}))\Psi_-(k) = \mp(-1)^{\nu - n}\frac{1}{2\mathrm{i}p_{2j}^3}\frac{\prod_{l=0}^{\nu}(p_{2j}^2 - q_{2l+1}^2)}{\prod_{\substack{l=1 \\ l \ne j}}^{n}(p_{2j}^2 - p_{2l}^2)}(1 \pm \mathrm{i}p_{2j})^{2(n-\nu)},$$

(see (31)) and

$$\Psi_-^r(-p_{2j}) = \overline{\Psi_-^r(p_{2j})}$$

for $j = 1, \ldots, n$. Since the poles of $w_-$ reside in the upper half of the complex plane, by application of the inverse Fourier transform and the residue theorem it is possible to determine the asymptotes for $\eta \to -\infty$ of the original function $w_r^{(j)}(\eta)$ in the form

$$w_r^{(j)}(\eta) \sim a\mathrm{i}\sum_{k^*}\mathrm{Res}(w_-(k)e^{-\mathrm{i}k\eta}, k^*), \quad \eta \to -\infty \tag{A.2}$$

where $k^* = \pm p_{2j} + 0\mathrm{i}$, $j = 1, \ldots, n$, are the simple poles of $w_-(k) \times e^{-\mathrm{i}k\eta}$. Therefore,

$$\begin{aligned} w_r^{(j)}(\eta) &= \frac{a\Psi_-^r(p_{2j})}{\mathrm{i}L_-(p_{2j})}\left[\frac{C e^{\mathrm{i}\phi}}{(p_{2j} - p_\nu)} + \frac{\overline{C} e^{-\mathrm{i}\phi}}{(p_{2j} + p_\nu)}\right]e^{-\mathrm{i}p_{2j}\eta} \\ &\quad - \frac{a\overline{\Psi_-^r(p_{2j})}}{\mathrm{i}\overline{L_-(p_{2j})}}\left[\frac{C e^{\mathrm{i}\phi}}{(p_{2j} + p_\nu)} + \frac{\overline{C} e^{-\mathrm{i}\phi}}{(p_{2j} - p_\nu)}\right]e^{\mathrm{i}p_{2j}\eta} \\ &= 2a\mathrm{Re}\left\{\frac{\Psi_-^r(p_{2j})}{\mathrm{i}L_-(p_{2j})}\left[\frac{C e^{\mathrm{i}\phi}}{(p_{2j} - p_\nu)} + \frac{\overline{C} e^{-\mathrm{i}\phi}}{(p_{2j} + p_\nu)}\right]e^{-\mathrm{i}p_{2j}\eta}\right\}. \end{aligned} \tag{A.3}$$

Thus from this we obtain (53)–(56).

*A.2.2. Derivation of the transmitted waves $w_{tr}^{(j)}$.* The transmitted waves appear from the residues of the poles of the function $w_+$ in (39) at $k = \pm q_{2j} - 0\mathrm{i}$, $1 \le j \le \nu$, provided $\nu > 0$ (otherwise no transmitted waves exist).

Consider the asymptotes of $w_+$ near $k = \pm q_{2j} - 0\mathrm{i}$. Then the leading order term in these asymptotes of $w_+$ is

$$\mathrm{i}\Psi_+^{tr}(\pm q_{2j})L_+(\pm q_{2j})\left[\frac{C e^{\mathrm{i}\phi}}{\pm q_{2j} - p_\nu} + \frac{\overline{C} e^{-\mathrm{i}\phi}}{\pm q_{2j} + p_\nu}\right]\frac{1}{0 - \mathrm{i}(k \mp q_{2j})}, \tag{A.4}$$

for $k \to \pm q_{2j} - 0\mathrm{i}$, with

$$\Psi_+^{tr}(\pm q_{2j}) = \lim_{k \to \pm q_{2j}} (0 - \mathrm{i}(k \mp q_{2j}))\Psi_+(k) = \mp(-1)^{n-\nu+1}\frac{1}{2\mathrm{i}q_{2j}}\frac{\prod_{l=1}^{n}(q_{2j}^2 - p_{2l-1}^2)}{\prod_{\substack{l=1 \\ l \ne j}}^{\nu}(q_{2j}^2 - q_{2l}^2)}\frac{1}{(1 \mp \mathrm{i}q_{2j})^{2(n-\nu)}}. \tag{A.5}$$

Next performing the inverse Fourier transform and the residue theorem, together with (A.4) and applying similar steps used in the previous section allows one to derive expressions (61)–(63).

*A.2.3. Derivation of the inclination behind the transition front.* The second order pole at $k = 0$ of the function $w_-$ produces a linear displacement behind the transition front as discussed in Section 4.2.2. To obtain the expressions for the slope shown there, consider the function

$$\mathfrak{M}(k) = w_-(k)(0 + \mathrm{i}k)^2 = \frac{\Psi_-^{sl}(k)}{L_-(k)}\left[\frac{C e^{\mathrm{i}\phi}}{0 + \mathrm{i}(k - p_\nu)} + \frac{\overline{C} e^{-\mathrm{i}\phi}}{0 + \mathrm{i}(k + p_\nu)}\right].$$

which is obtained from (40). The function $\Psi_-^{sl}$ in (60) has the following asymptote near $k = 0$:

$$\Psi_-^{sl}(k) = \Psi_-^{sl}(0) + k(\Psi_-^{sl})'(0) + O(k^2)$$

for $k \to 0$ with

$$\Psi_-^{sl}(0) = \frac{\prod_{j=0}^{\nu} q_{2j+1}^2}{\prod_{j=1}^{n} p_{2j}^2}, \quad (\Psi_-^{sl})'(0) = -2\mathrm{i}(\nu - n)\frac{\prod_{j=0}^{\nu} q_{2j+1}^2}{\prod_{j=1}^{n} p_{2j}^2}.$$

Also note

$$\begin{aligned} &\frac{1}{L_-(k)}\left[\frac{C e^{\mathrm{i}\phi}}{0 + \mathrm{i}(k - p_\nu)} + \frac{\overline{C} e^{-\mathrm{i}\phi}}{0 + \mathrm{i}(k + p_\nu)}\right] \\ &= -\frac{2\mathrm{Im}(C e^{\mathrm{i}\phi})}{p_\nu L_-(0)} + \frac{2\mathrm{i}}{p_\nu L_-(0)} \\ &\quad \times\left[\frac{\mathrm{Re}(C e^{\mathrm{i}\phi})}{p_\nu} + \frac{\mathrm{Im}(L_-'(0))}{L_-(0)}\mathrm{Im}(C e^{\mathrm{i}\phi})\right]k + O(k^2). \end{aligned}$$

Thus, computing the Taylor expansion of $\mathfrak{M}(k)$ near $k = 0$ we have to first order:

$$\mathfrak{M}(k) = \mathfrak{M}(0) + k\mathfrak{M}'(0) + O(k^2), \quad \text{for} \quad k \to 0,$$

where

$$\mathfrak{M}(0) = -\frac{2\mathrm{Im}(C e^{\mathrm{i}\phi})\Psi_-^{sl}(0)}{p_\nu L_-(0)} \tag{A.6}$$

and

$$\mathfrak{M}'(0) = -\frac{2\mathrm{Im}(C e^{\mathrm{i}\phi})(\Psi_-^{sl})'(0)}{p_\nu L_-(0)} + \frac{2\mathrm{i}\Psi_-^{sl}(0)}{p_\nu L_-(0)}\left[\frac{\mathrm{Re}(C e^{\mathrm{i}\phi})}{p_\nu} + \frac{\mathrm{Im}(L_-'(0))}{L_-(0)}\mathrm{Im}(C e^{\mathrm{i}\phi})\right]. \tag{A.7}$$

This then provides the asymptote of $w_-$ near $k = 0$ in the form:

$$w_-(k) = \frac{1}{(0 + \mathrm{i}k)^2}\left[\mathfrak{M}(0) + k\mathfrak{M}'(0)\right] + O(1).$$

Application of the inverse Fourier transform and the residue theorem, for $\eta \to -\infty$, then yields

$$w_s(\eta) = -\mathrm{i}\mathfrak{M}'(0) - \mathfrak{M}(0)\eta,$$

and this with (A.6) and (A.7) gives (57)–(60).

## References


Bažant, Z.P., Verdure, M., 2007. Mechanics of progressive collapse: learning from World Trade Center and building demolitions. J. Eng. Mech. 133, 308–319.

Behn, C., Marder, M., 2015. The transition from subsonic to supersonic cracks. Philos. Trans. R. Soc. A. 373, 20140122.

Bouchbinder, E., Fineberg, J., Marder, M., 2010. Dynamics of simple cracks. Annu. Rev. Condens. Matter Phys. 1, 371–395.

Brun, M., Movchan, A.B., Slepyan, L.I., 2013. Transition wave in a supported heavy beam. J. Mech. Phys. Solids 61, 2067–2085.

Craster, R.V., Kaplunov, J., Postnova, J., 2010. High frequency asymptotics, homogenisation and localisation for lattices. Q. J. Mech. Appl. Math. 63 (4), 497–518.

Deegan, R.D., Chheda, S., Patel, L., Marder, M., Swinney, H.L., Jeehoon, K., de Lozanne, A., 2003. Wavy and rough cracks in silicon. Phys. Rev. E 67, 066209.

Guozden, T.M., Jagla, E.A., Marder, M., 2010. Supersonic cracks in lattice models. Int. J. Fract. 162, 107–125.

Kawashima, K., Takahashi, Y., Ge, H., Wu, Z., Zhang, J., 2009. Reconnaissance report on damage of bridges in 2008 Wenchuan, China, earthquake. J. Earthq. Eng. 13, 965–996.
Kozlov, V.A., Maz'ya, V.G., Movchan, A.B., 1995. Asymptotic representation of elastic fields in a multi-structure. Asymptot. Anal. 11, 343–415.
Liu, Y., Bing, H., Xiao, Ma, 2011. Advances in progressive collapse of bridge structures. Pac. Sci. Rev. 13 (3), 173–181.
Marder, M., 2004. Effects of atoms on brittle fracture. Int. J. Fract. 130, 517–555.
Marder, M., Gross, S., 1995. Origin of crack tip instabilities. J. Mech. Phys. Solids 43 (1), 1–48.
Mishuris, G.S., Movchan, A.B., Bigoni, D., 2012. Dynamics of a fault steadily propagating within a structural interface. Multiscale Model. Simul. 10 (3), 936–953.
Mishuris, G.S., Movchan, A.B., Slepyan, L.I., 2008a. Dynamical extraction of a single chain from a discrete lattice. J. Mech. Phys. Solids 56, 487–495.
Mishuris, G.S., Movchan, A.B., Slepyan, L.I., 2008b. Dynamics of a bridged crack in a discrete lattice. Q. J. Mech. Appl. Math. 61 (2), 151–160.
Mishuris, G.S., Movchan, A.B., Slepyan, L.I., 2009a. Localised knife waves in a structured interface. J. Mech. Phys. Solids 57, 1958–1979.
Mishuris, G.S., Movchan, A.B., Slepyan, L.I., 2009b. Localization and dynamic defects in lattice structures. In: CISM, International Centre for Mechanical Sciences (Ed.), Computational and Experimental Mechanics of Advanced Materials. Springer, pp. 51–82.
Movchan, A.B., Brun, M., Slepyan, L.I., Giaccu, G.F., 2015. Dynamic multi-structure in modelling a transition flexural wave. Mathematika 61, 444–456.
Nieves, M.J., Movchan, A.B., Jones, I.S., Mishuris, G.S., 2013. Propagation of Slepyan's crack in a non-uniform elastic lattice. J. Mech. Phys. Solids 61, 1464–1488.
Noble, B., 1958. Methods Based on the Wiener–Hopf Technique for the Solution of Partial Differential Equations. International Series of Monographs on Pure and Applied Mathematics 7. Pergamon Press, New York.
Panasenko, G.P., 2005. Multi-Scale Modelling for Structures and Composites. Springer.
Ryvkin, M., Slepyan, L., 2010. Crack in a 2D beam lattice: analytical solutions for two bending modes. J. Mech. Phys. Solids 58, 902–917.
Slepyan, L.I., 1981. Dynamics of a crack in a lattice. Sov. Phys. Dokl. 26, 538–540.
Slepyan, L.I., 2001a. Feeding and dissipative waves in fracture and phase transition. I. Some 1D structures and a square-cell lattice. J. Mech. Phys. Solids 49, 469–511.
Slepyan, L.I., 2001b. Feeding and dissipative waves in fracture and phase transition. III. Triangular-cell lattice. J. Mech. Phys. Solids 49, 2839–2875.
Slepyan, L.I., 2002. Models and Phenomena in Fracture Mechanics. Springer, Berlin.
Slepyan, L.I., 2010a. On discrete models in fracture mechanics. Mech. Solids 45 (6), 803–814. doi:10.3103/S0025654410060051.
Slepyan, L.I., 2010b. Wave radiation in lattice fracture. Acoust. Phys. 56 (6), 962–971. doi:10.1134/S1063771010060217.
Slepyan, L.I., Ayzenberg-Stepanenko, M.V., Mishuris, G.S., 2015. Forerunning mode transition in a continuous waveguide. J. Mech. Phys. Solids 78, 32–45. http://dx.doi.org/10.1016/j.jmps.2015.01.015.
Slepyan, L.I., Movchan, A.B., Mishuris, G.S., 2010. Crack in a lattice waveguide. Int. J. Fract. 162, 91–106.
Slepyan, L.I., Troyankina, L.V., 1984. Fracture wave in a chain structure. J. Appl. Mech. Tech. Phys. 25 (6), 921–927.